December 2017

Improving Hyperspectral Subpixel Target Detection Using Hybrid Detection Space

Ruixing Li
University of Nevada, Las Vegas

Repository Citation

Li, Ruixing, "Improving Hyperspectral Subpixel Target Detection Using Hybrid Detection Space" (2017). *UNLV Theses, Dissertations, Professional Papers, and Capstones*. 3147.
http://dx.doi.org/10.34917/11889717

IMPROVING HYPERSPECTRAL SUBPIXEL TARGET DETECTION USING HYBRID DETECTION SPACE

By

Ruixing Li

Bachelor of Engineering
South China Normal University, China
2007

A Thesis Submitted in partial fulfillment
of the requirements for the

Masters of Science in Engineering-Electrical Engineering

Department of Electrical and Computer Engineering
Howard R. Hughes College of Engineering
The Graduate College

University of Nevada, Las Vegas
December 2017

UNLV | GRADUATE COLLEGE

Thesis Approval

The Graduate College
The University of Nevada, Las Vegas

August 11, 2017

This thesis prepared by

Ruixing Li

entitled

Improving Hyperspectral Subpixel Target Detection Using Hybrid Detection Space

is approved in partial fulfillment of the requirements for the degree of

Masters of Science in Engineering-Electrical Engineering
Department of Electrical and Computer Engineering

Shahram Latifi, Ph.D.
Examination Committee Chair

Sahjendra Singh, Ph.D.
Examination Committee Member

Pushkin Kachroo, Ph.D.
Examination Committee Member

Laxmi Gewali, Ph.D.
Graduate College Faculty Representative

Kathryn Hausbeck Korgan, Ph.D.
Graduate College Interim Dean

ABSTRACT

A Hyper-Spectral Image (HSI) has high spectral and low spatial resolution. As a result, most targets exist as subpixels, which pose challenges in target detection. Moreover, limitation of target and background samples always hinders the target detection performance. In this thesis, a hybrid method for subpixel target detection of an HSI using minimal prior knowledge is developed. The Matched Filter (MF) and Adaptive Cosine Estimator (ACE) are two popular algorithms in HSI target detection. They have different advantages in differentiating target from background. In the proposed method, the scores of MF and ACE algorithms are used to construct a hybrid detection space. First, some high abundance target spectra are randomly picked from the scene to perform initial detection to determine the target and background subsets. Then, the reference target spectrum and background covariance matrix are improved iteratively, using the hybrid detection space. As the iterations continue, the reference target spectrum gets closer and closer to the central line that connects the centers of target and background and resulting in noticeable improvement in target detection. Two synthetic datasets and two real datasets are used in the experiments. The results are evaluated based on the mean detection rate, Receiver Operating Characteristic (ROC) curve and observation of the detection results. Compared to traditional MF and ACE algorithms with Reed-Xiaoli Detector (RXD) background covariance matrix estimation, the new method shows much better performance on all four datasets. This method can be applied in environmental monitoring, mineral detection, as well as oceanography and forestry reconnaissance to search for extremely small target distribution in a large scene.

ACKNOWLEDGEMENT

The first course I took at the University of Nevada, Las Vegas was “Coding with Applications in Computers and Communication Media” instructed by Dr. Shahram Latifi. This course triggered my enthusiasm in mathematics which had been concealed for many years. My master study at UNLV is memorable for me, for it is a valuable experience to learn some advanced knowledge in both engineering and math. I am grateful to many people who help me accomplish it.

I would like to express my great gratitude to my advisor, Dr. Shahram Latifi. Without his help, my graduate study in the U.S. would not become true. He is a gracious professor and dedicated researcher. I would like to thank him for his encouragement, guidance and support during my master study.

I would like to thank Dr. Yahia Baghzouz for his kind support and insightful instruction. I would also like to thank Dr. Sahjendra Singh, Dr. Laxmi Gewali and Dr. Pushkin Kachroo for serving as my committee members and providing helpful instructions.

This research is partially supported by the National Science Foundation under Grant No.IIA-1301726. I would like to acknowledge the National Science Foundation, Roy & Helen Kelsall Engineering Scholarship and UNLV Graduate Access Grant for the financial support.

I would also like to thank NASA/JPL-Caltech and the University of the Basque Country for providing the HSI datasets used in the experiments.

Finally, I would like to thank Ms. Meagan Madariaga-Hopkins for helping me review the thesis, Mr. Christopher Hicks and Mr. Shahab Tayeb for their encouragement and help both in study and life.

TABLE OF CONTENTS

LIST OF FIGURES

LIST OF TABLES

NOTATIONS AND ACRONYMS

x	input pixel	ELM	empirical line method
A	atoms	GLRT	generalized likelihood ratio test
α	abundance	HSI	hyperspectral image
E	error	HU	hyperspectral unmixing
S	target spectral	HYDICE	hyperspectral digital imagery collection experiment
μ	average vector	ICA	independent component analysis
D	detector	LLM	linear mixing model
H_0	target absent hypothesis	MF	matched filter
H_1	target present hypothesis	MLE	maximum likelihood estimation
η	threshold	MODTRAN	MODerate resolution atmospheric TRANsmission
C_b	background covariance matrix	MSD	matched subspace detector
n	Gaussian random noise	MVN	multivariate normal distribution
N	distribution	NMF	nonnegative matrix factorization
		NP	Neyman–Pearson
ACE	adaptive coherence/cosine estimator	OSP	orthogonal subspace projection
ANC	abundance nonnegativity constraint	PCA	principal component analysis
ASC	abundance sum-to-one constraint	PDF	probability density function
ASD	adaptive subspace detector	PPI	pixel purity index
AVIRIS	airborne visible/infrared imaging spectrometer	ROC	receiver operator characteristic
CEM	constrained energy minimization	RXD	Reed–Xiaoli detector
CFAR	constant false alarm rate	SAM	spectral angle mapper
CG	convex geometry	SOMP	simultaneous orthogonal matching pursuit
DR	detection rate	UAV	unmanned aerial vehicle

1. INTRODUCTION

1.1 The importance of HSI target detection

Traditional remote detection uses single wavelength or RGB image in target detection, and target features can attenuate after long distance transmission and become insignificant. Hyperspectral sensors measure the radiance values of each pixel in the visible and short wave infrared regions with high spectral resolution that can be as low as 5-10 nm. As shown in Figure 1.1, HSI consists of hundreds of bands that can reflect the absorption and reflection property of certain materials, thus, any subtle variation in the spectra may imply possible existence of a target. As each material has its own spectral characteristics, high accuracy in spectral space helps to differentiate the small variance between pixels, offering a better opportunity in target and abnormal detection. Furthermore, the HSI camera can operate in a remote distance, such as satellite and Unmanned Aerial Vehicle (UAV), mostly at a height over 500 m. Remote detection, which avoids direct contact with hazardous materials, would be safer than direct contact detection methods. In addition, HSI does not require an active source used to illuminate the scene making it easier for implementation in a wide area.

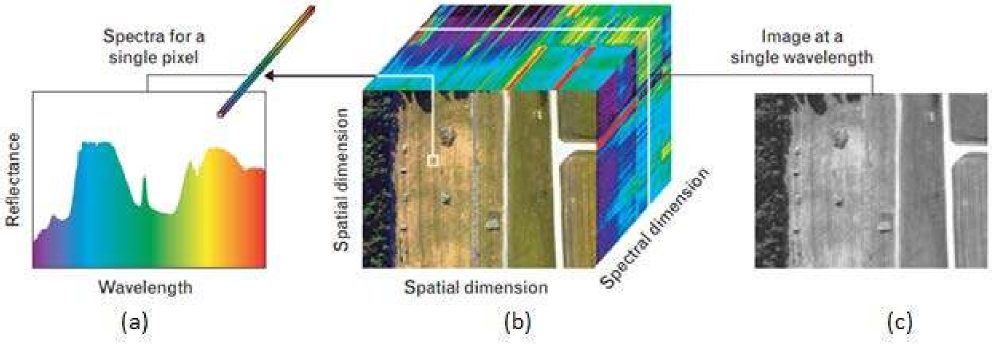

Figure 1.1: Hyperspectral data-cube
(a) Visualized as a set of spectra each for a single pixel; (b) Basic data-cube structure; (c) Visualized as a stack of images each for a single spectra channel [1]

HSI target detection is the method to search materials with a specific spectral signature to locate and identify hazardous materials or targets of interest [2]. High resolution in spectra enables target detection and identification based on comparing the material reflectance properties to the standard library. Some organizations have collected various material spectral samples to build standard spectral libraries for matching purposes. HSI target detection has been widely applied in environmental monitoring, mine detection, geographic airborne searches, rescue operations, oceanography and forestry reconnaissance. Its strong ability has been proven in public safety and defense applications.

As the HSI camera becomes less expensive, HSI is also applied in food production, medical examination, transportation infrastructure inspection and many other fields. The need for high quality detection algorithms is as important as development and improvement of the hardware. With the advance of remote detection techniques, HSI is attracting more and more attention as a complement detection method along with traditional ones.

1.2 Development of HSI detection algorithms

Multispectral image (MSI) has been studied since the 1970s, and in recent years, MSI and HSI have been introduced to many applications in various fields. HSI is much better in remote detection than the traditional methods because imagery beyond the visual allows more information to be extracted from a scene. More and more scholars are attracted to HSI research. The United States Geological Survey (USGS) has built the spectral database since the 1980s. The Airborne Visible/Infrared Imaging Spectrometer (AVIRIS) developed by NASA's Jet Propulsion Laboratory and Hyperspectral Digital Image Collection Experiment (HYDICE) sensor developed by the Naval Research Laboratory have achieved great success and been widely used for target detection.

The Linear Mixing Model (LMM) [3] introduced in 1986 became the cornerstone for hyperspectral image analysis. The LMM assumes all the pixels consist of non-overlapping materials. Then, Craig invented Convex Geometry (CG) for Hyperspectral Unmixing (HU) in the early 1990s [4]. Many pioneers such as Boardman made great contributions to CG-based blind HU. Among them, is Winter, who proposed the maximization of simplex volume to solve for the spectra of endmembers, which is the famous N-FINDR algorithm [5], still popular today. These models then became the fundamental basis for HSI research.

Most detection algorithms are based on the Multi-Variate Normal (MVN) distribution assumption of background and target distribution, and then the Generalized Likelihood Ratio Test (GLRT) is applied to find whether the test pixel is a target according to the Probability Density Function (PDF) of the target and background on the specific test pixel. In anomaly detection, pixels that have a significantly different spectral signature from their neighboring background clutter pixels are defined as spectral anomalies [6]. Reed and Yu proposed the famous RX anomaly detector in 1990 [7]. This well-known detector, which has been successfully applied to many hyperspectral target detection applications, is based on the MVN distribution of background. The RX detector is a CFAR adaptive anomaly detector which is derived from the GLRT [8] and now considered as the benchmark anomaly detection algorithm for HSI [9]. A number of hyperspectral detection techniques have been developed to address the spectral variability and spectral mixing issues either jointly or separately [10]. Many target detection algorithms have been developed to meet these needs. The Spectral Angle Mapper (SAM) developed by Boardman in 1993 is the simplest algorithm that is not based on any assumption of data distribution [11, 12]. It has low computation cost but is not capable for subpixel target detection. Then the Matched Filter (MF) based on statistics distribution was proposed to improve detection performance for subpixel targets

[13]. In 1995, a more powerful algorithm, Adaptive Cosine Estimator (ACE) [14], which also derived from the GLRT, was introduced to strengthen the detection performance for extremely small subpixel targets.

Besides the statistical model, another popular model for target detection is the subspace model. In the subspace model, any pixel consists of a linear combination of target subspace and background subspace. The Matched Subspace Detector (MSD) [15] and the Adaptive Subspace Detector (ASD) [16] are algorithms based on the subspace model [12]. The MSD employs the LMM model for the subpixel target detection. Background and target pixels correspond to target absent (H_0) and target present (H_1) hypotheses, respectively. Then, the Maximum Likelihood Estimation (MLE) is used to evaluate the existence of a target. Some approaches use array processing techniques to nullify the background signatures as one would nullify an interfering signature when performing beamforming [17]. The Orthogonal Subspace Projection (OSP) algorithm [18], developed by Harsanyi and Chang in 1994, is an example of such methods. The OSP is used to deal with subpixel signals, separating desired spectral signals from the undesired spectra [10].

In recent years, one other kind of approach for target detection has emerged. This kind of method directly sets a threshold for the target abundance values of the pixels. Examples of this type of approach include the fully constrained least squares algorithm and representation methods [19, 20, 21]. The Sparse Representation-based Detector (SRD), originally developed for face recognition, has attracted considerable attention in the past ten years [22]. Sparse representation was first proposed to solve computer vision tasks with the assumption that pixels belonging to the same class should lie in the same low-dimensional subspace [23]. In 2011, Chen introduced sparse representation to HSI target detection and classification, which leads to good performance [23, 24]. The essence of the SRD is built on the concept that a pixel can be represented as a linear combination of labeled samples via the sparse regularization techniques, such as the l_0-norm regularization and the l_1-norm regularization [22]. Another similar algorithm is the Collaborative Representation Detector (CRD) proposed by Li in 2015 [21], which represents the test pixel as a linear combination of all the training samples. The CRD also plays an important role in HSI target detection [25].

HSI usually has the similar spectral properties in the neighboring region. Therefore, combining contextual information in the post processing stage can improve the detection performance greatly. More and more detection methods have used joint spatial-spectral features to improve the detection performance [26]. In addition to the constraints on sparsity and reconstruction accuracy, spatial smoothness across neighboring HSI pixels are often taken into consideration [27]. Two models have been proposed to apply contextual information to the SRD method: Simultaneous Orthogonal Matching Pursuit (SOMP) and Orthogonal Matching Pursuit-Smooth (OMP-S). SOMP supposes neighboring pixels can be simultaneously represented by common atoms, while OMP-S is with smoothing constraints that force vector Laplacian to be close to zero. In CRD, Joint Collaborative Representation (JCR) seeks to incorporate the contextual information during classification [26]. Similar to SOMP and OMP-S, JCR incorporates spatial information into the algorithms. The neighboring pixels are assumed to be a linear combination of some common samples from the training dictionary but have different weights [23].

In real HSI, due to the existence of man-made objects or other factors, the data do not always have a linear property. The kernel method was first introduced to address the nonlinear properties of data structure by Kwon in 2005 [9]. The original data is transformed into a high-dimensional feature space, which consists of many nonlinear combinations of the original spectra. This process enhances the discrimination between classes and makes the decision simpler. Therefore, the kernel method has been applied to different detection algorithms to address the nonlinear properties of HSI and improve the detection performance.

1.3 Challenges

1.3.1 Subpixel detection

Although HSI has high resolution in spectral space, it does not have good resolution in spatial space, roughly 1 m -3.6 m per pixel for aerial HSI. Due to the long distance from the scene and low spatial resolution [28], mixed pixels broadly exist. This increases the difficulty in the detection process.

The challenge in detecting low abundance subpixel targets is how to separate the target's spectral signature from majority mixture signatures of background within the pixel [17]. Although HSI data have low spatial resolution, their rich spectral information can compensate for this. Under high spectral resolution, targets of interest present as some data abnormalities. Using this information, subpixel or low abundance targets can be detected.

1.3.2 Uncertainty of spectra

It is observed that although two pixels consist of the same material, their spectra may vary (Figure 1.2). On the other hand, different materials may show similar spectra. These phenomena are called spectral variation. Spectral variation widely exists because of the random properties of the transmission environment. Illumination and atmosphere are the main factors contributing to spectral variation.

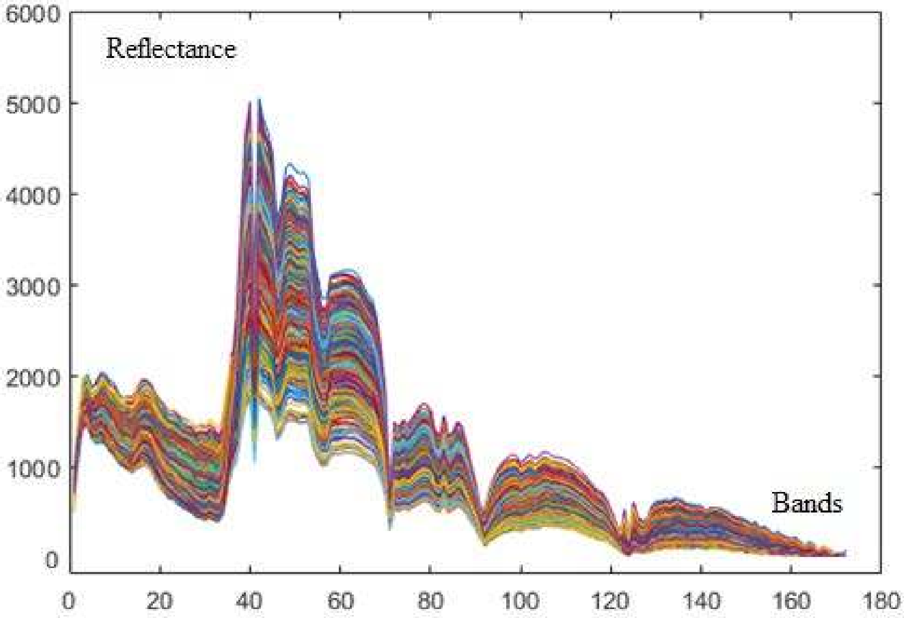

Figure 1.2: Variation of water spectral curves extracted from Moffett Field image

In application of HSI target detection, a relative pure spectral signature is usually needed. Currently, researchers obtain the spectral curve from one of two methods: a standard spectral library or HU from the data. The standard library, as mentioned before, is built by organizations like the USGS through many years of accumulation. The fixed target signature from the standard library could be quite different from the target spectral extracted from the scene [29] because of the interference of many factors such as illumination, gas, vapor, and aerosol, as well as the interaction among pixels. This would nullify the prior spectral signature in the spectral library and finally affect the detection results. To improve the detection performance, researchers have used a preprocessing stage to compensate for the impacts of atmospheric influence. These techniques can convert original data to the same domain as the library spectra.

However, the reference signatures in the standard library would be useless if high inference happens. In real practice, extracting the endmember of interest (the pure material spectral curve) from the scene would be better than using the target signature from the standard library. Extracting the material spectral curve and calculating the corresponding abundance is called Hyperspectral Unmixing (HU). The extracted spectral curve is then used to fulfill target detection or classification. The limitation of HU is the need to estimate the number of endmembers before unmixing. Different estimations would lead to quite different results. Furthermore, as most HU algorithms are based on the CG assumption, the lack of full pixels of interest would lead to inaccuracy in the extracted target spectral signature.

Using a single sample spectral curve extracted from the scene for target detection would also cause low detection performance due to uncertainty of spectra. Acquiring spectral data in different conditions and studying the principles of spectral variation can improve target detection performance. Some researchers try to use multiple signatures to capture the variational nature of target spectra [29]. The physics-based model MODTRAN has been introduced to extract the target spectra and exclude the environmental interference. In subspace detection algorithms, these target signature samples span as a subspace which can better represent the target.

1.3.3. Background estimation

One critical challenge in detecting targets and anomalies is to describe the background with minimum interference of targets. Classical background models such as MVN distribution [30] and subspace models have led to many target detection algorithms [31]. However, a considerable mismatch is observed between these simple models and the complicated properties of the HSI background. In the MVN model, the estimate covariance matrix may be ill conditioned due to the contamination of subpxiel targets, and noise as well as a high correlation between bands. In the subspace model, uncompleted background endmembers would also have deleterious effects in constraining the background signals. Therefore, more complex models should be developed to meet the needs of low abundance subpixel target detection.

1.4 Summary

As the HSI technique is applied in more and more areas, traditional target detection methods based on the standard library or extracting the target spectrum using HU may not still be applicable. The goal of this thesis is to improve the subpixel target detection performance with minimal prior knowledge.

The remainder of this thesis is organized as following: Chapter II introduces the fundamental theories of HSI analysis; Chapter III discusses about the HSI pre-processing algorithms that are widely used for traditional HSI detection methods; basic target detection algorithms are introduced in Chapter IV; the proposed method based on hybrid detection space is discussed in Chapter V; experimental models, results and discussions are provided in Chapter VI; conclusions of this thesis are presented in Chapter VII.

2. HSI FUNDAMENTALS

2.1 HSI representation

There are three common representations for HSI: image space, spectral space and feature space (Figure 2.1). These methods can help in visualization of the abstruse HSI dataset, and make it easier for analysis. Image space describes the brightness versus the pixel coordinates for a given band. Spectral space describes the brightness versus spectral bands for a given pixel. In feature space, different materials are represented by two principal bands which can differentiate the main features of the materials. Similar to feature space, detection space in which two axes are the scores of two different algorithms, is introduced in Chapter V.

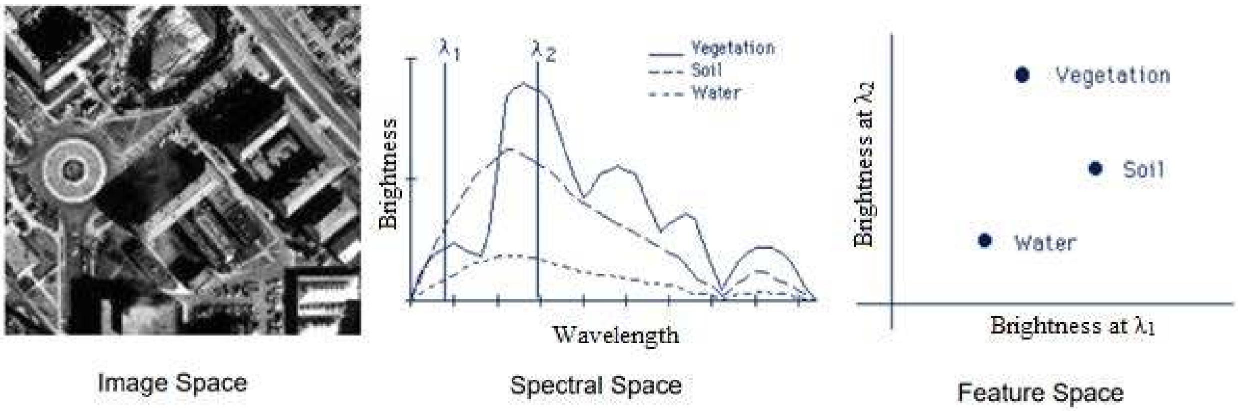

Figure 2.1: The forms for representing hyperspectral data [32]

2.2 Linear mixing model

The research of HSI starts with a data model. Currently, there are mainly two data models: the Linear Mixing Model (LMM) and the nonlinear model. The assumption for LMM is that the spectra are represented by unique, spatially-nonoverlapping materials (Figure 2.2) [33]. The interaction between endmembers is ignored. The LMM is the corner stone for most subpixel detection algorithms [17]. It has been proven that the LMM can achieve satisfactory decomposed results and is the most useful model.

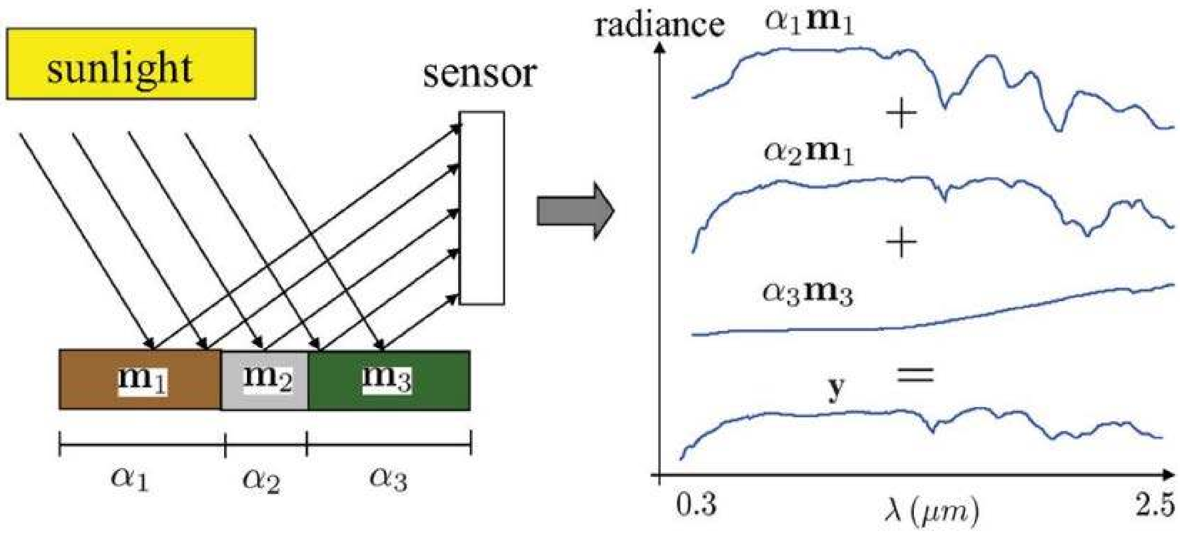

Figure 2.2: Linear Mixing Model [34]

The LMM assumes that any pixel is a linear combination of target and background endmembers. Abundances are the percentages of each endmember for a given pixel [35]. Obviously, each pixel must be a combination of certain endmembers, and Abundances must satisfy the Sum-to-one Constraint (ASC) and the Abundance Nonnegative Constraint (ANC) [36]. Mathematically, the LMM is written as [17]:

$$x=A\alpha+E,\ \alpha_i>=0,\ \sum_{i=1}^{M}\alpha_i = 1 \qquad (2.1)$$

where x is a vector that represents the spectra of a specific pixel, M is the number of endmembers; $\boldsymbol{A}$ is a matrix where each column represents each endmember; α is a vector where the entries represent the corresponding abundance value α_i for the i_{th} endmember; E is an error vector.

The LMM assumes that the photons received by the camera only react with one material. On the other hand, the nonlinear mixing model believes that the photons have reacted with different materials before entering the sensor. In real practice, linear mixing and nonlinear mixing coexist. Considering from an energy perspective, due to the energy of the photon, which reflects multiple times being so weak, it can be ignored most of the time. Normally, researchers only consider that the photon reacts with the first material. In this way, the complex nonlinear model can be simplified to the LMM.

The LMM has a simple structure and defined physical meaning and can satisfy the accuracy requirement for most cases. Therefore, the LMM has been broadly applied in HSI analysis. Currently, most endmember extraction and target detection algorithms are based on the LMM.

2.3 Background description model

In most HSI algorithms, varieties of backgrounds are described in two modeling strategies: statistic and subspace.

2.3.1 Statistical model

Inspection of several density scatter plots suggests that a plausible model for the PDF of hyperspectral data is the density mixture [37, 38]:

$$f(x) = \sum_{k=1}^{N} \pi_k f_k(x), \pi_k \geq 0, \sum_{k=1}^{N} \pi_k = 1, \tag{2.2}$$

where $f_k(x)$ is the PDF of kth class; π_k is a priori probability of *k*th class; *N* is the number of classes. Normally, when N=1, natural hyperspectral backgrounds have heavy-tail behavior. The multivariate *t*-Elliptically Contoured Distribution (*t*-ECD) can capture the heavy-tail behavior of $f_k(x)$ [1]. As N increases, each band approximately follows a normal distribution (Figure 2.3). As a result, the HSI distribution tends towards the MVN distribution (Figure 2.4) and has lighter tails. The MVN distribution of a k-dimensional random vector x = [X_1, $X_{2\ldots}$ X_k] can be written in the following notation [39, 40]:

$$x \sim \mathcal{N}(\mu, C_b),$$

with a *k*-dimensional mean vector:

$$\mu = E(x) \tag{2.3}$$

and a *k*×*k* covariance matrix:

$$C_b =: E[(x-\mu)(X-\mu)^T] = [Cov[X_i, X_j]; 1 \leq i, j \leq k] \tag{2.4}$$

Because each class approximately follows normal distribution, if the symmetric covariance matrix $\boldsymbol{C_b}$ is positive definite, the distribution density f_x of a random vector x would be [39]:

$$f_x(x_1, \dots, x_{k)} = \frac{\exp(-\frac{1}{2}(x-\mu)^T C_b^{-1}(x-\mu))}{\sqrt{(2\pi)^k |C_b|}} \tag{2.5}$$

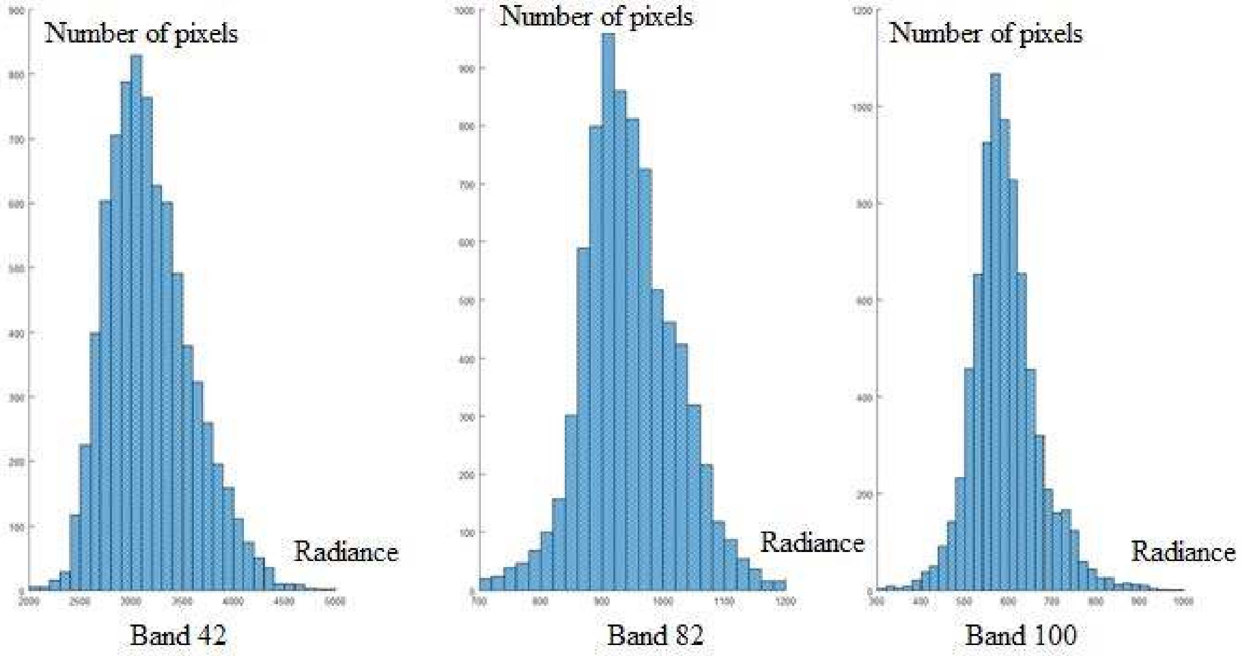

Figure 2.3: Histogram of Band 42 82 100 for the Moffett Field image

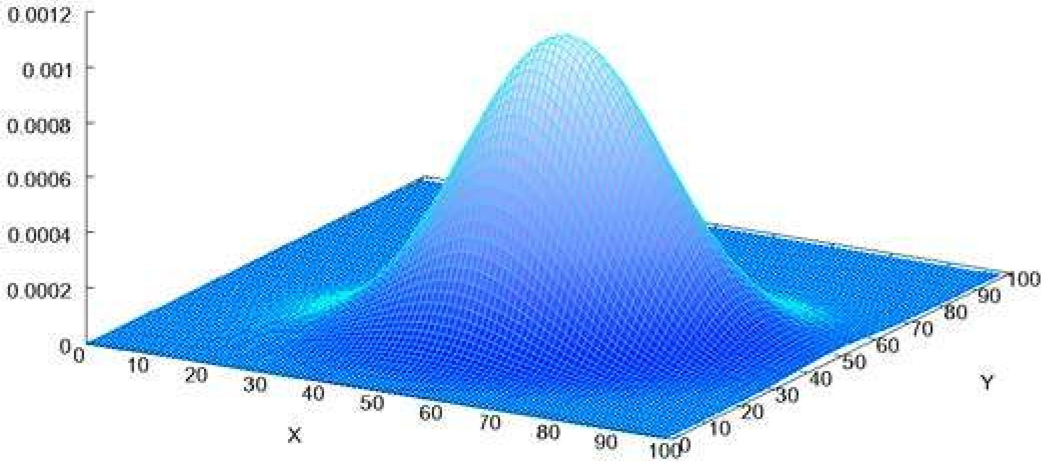

Figure 2.4: An example of multivariate normal distribution [39]

2.3.2 Subspace model

The background is assumed to lie in a low-dimensional subspace in the subspace model [27]. The pixel spectrum is represented by a linear combination of background and target endmembers in its low-dimensional subspace. The distribution of background does not matter in this model. A target-free pixel x, which is consistent with the null hypothesis, can be written as [31]:

$$x=B\beta+n \tag{2.6}$$

where B defines the background subspace; β specifies the coefficients of the linear combination of vectors in B; and n is a “lack of fit” noise term that should be of small magnitude if the model is accurate [31]. The target is assumed to be somewhat orthogonal to the background subspace. Projecting the pixels to be tested into the subspace orthogonal to the background subspace and observing the residuals can enhance the detection of target signals:

$$\hat{n}_0 = (I - P_B)x \tag{2.7}$$

where $P_B = B(B^T B)^{-1} B^T$ is a projection matrix associated with the N_b-dimensional background subspace <B> [41]. The OSP detector is based on the subspace model, for a given pixel x:

$$x = s\alpha + B\beta + n \tag{2.8}$$

where s is the desired target; B is the known background subspace; the columns of B are the undesired background endmember spectra; n is noise. The output of the OSP detector is [29]:

$$D_{OSP} = q_{OSP}^{T} x = s^{T} P_{B}^{\perp} x \tag{2.9}$$

where $q_{OSP}^{T} = s^{T} P_{B}^{\perp}$is the OSP operator consisting of a background spectral signature rejecter $P_{B}^{\perp} = (I - P_{B})$ followed by a matched filter [29]. The OSP nullifies the background signatures using the spectral matching filter q_{OSP}^{T}. Its detection process is as follows (Figure 2.5):

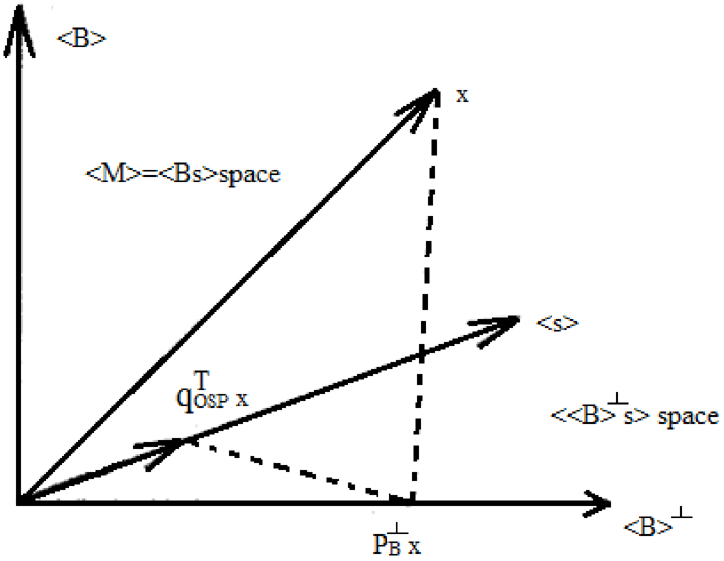

Figure 2.5: Orthogonal projection spaces, modified from [42]

First the target data x is projected in the subspace orthogonal to the background subspace <B> by using the orthogonal complement projector $P_{B}^{\perp}$. Then the residual projects to the target subspace <s>. Finally, the test pixel x is decomposed into two parts: the desired signature of interest s, and undesired signature matrix B [43]. In the HSI, background and target spectra are not constant all the time. It is more accurate to describe the background and target in a subspace rather than using only one spectrum. While looking for multiple targets, a subspace detector needs to be employed. However, even increasing the size of the subspace slightly, the number of combinations of signatures increases quickly, resulting in retrieving more pixels and obtaining a higher FAR. Besides that, the OSP is also quite sensitive to noise.

2.4 Neyman-Pearson criterion and Generalized Likelihood Ratio Test (GLRT)

In statistics, the Neyman–Pearson(NP) lemma, named after Jerzy Neyman and Egon Pearson, states that when performing a hypothesis test $\Lambda(x)$ between two simple hypotheses, $f_0(x|H_0)$ is the conditional PDF of observing x under the H_0 hypothesis and $f_1(x|H_1)$ is the PDF of observing x under the H_1 hypothesis [1, 37, 39, 44], the Likelihood-Ratio Test (LRT) rejects H_0 in favor of H_1 only if $\Lambda(x)$ exceeds a certain threshold η, otherwise, the H_0 is accepted. $\Lambda(x)$ can be represented as:

$$\Lambda(x) = \frac{f_1(x|Target\ present)}{f_0(x|Target\ absent)} \triangleq \frac{f_1(x|H_1)}{f_0(x|H_0)} \gtrless_{H_0}^{H_1} \eta \tag{2.10}$$

For example, in Figure 2.6, p_1 is the PDF of the H_1 hypothesis at x_1 and p_0 is the PDF of the H_0 hypothesis at x_1. Then, a threshold can be set for p_1/p_0 to determine whether x_1 belongs to H_1. The Detection Rate (DR) and False Alarm Rate (FAR) are defined as:

$$DR = \frac{N_{hit}}{N_t} = \frac{\int_{x1}^{\infty} f_1(x|H_1)dx}{\int_{-\infty}^{\infty} f_1(x|H_1)dx} \ and\ FAR = \frac{N_{miss}}{N_{tot}} = \frac{\int_{x1}^{\infty} f_0(x|H_0)dx}{\int_{-\infty}^{\infty} f_0(x|H_0)dx} \tag{2.11}$$

where *Nhit* represents the number of targets detected; *Nt* stands for the total number of targets; *Nmiss* is the number of backgrounds detected as targets; *Ntot* is the total number of background pixels; and f_1, f_0 is the PDF of target and background, respectively. The DR becomes one when all the target pixels are detected [45]. The NP criterion can maximize the DR while keeping the FAR under a certain predetermined value.

To calculate $\Lambda(x)$, $f_1(x|H_1)$ and $f_0(x|H_0)$ are needed. However, in real practice, $f_i(x|H_i)$ often depends on some unknown parameter θ, which relates to the hypothesis model. The Generalized Likelihood Ratio Test (GLRT) is based on the MVN distribution assumption of the background. If θ is nonrandom, the GLRT under each hypothesis is:

$$\Lambda_G \triangleq \frac{f_1(x|\hat{\theta}_1,H_1)}{f_0(x|\hat{\theta}_0,H_0)} \gtrless_{H_0}^{H_1} \eta,\ \hat{\theta}_i = \max f_i(x|\theta,H_i) \tag{2.12}$$

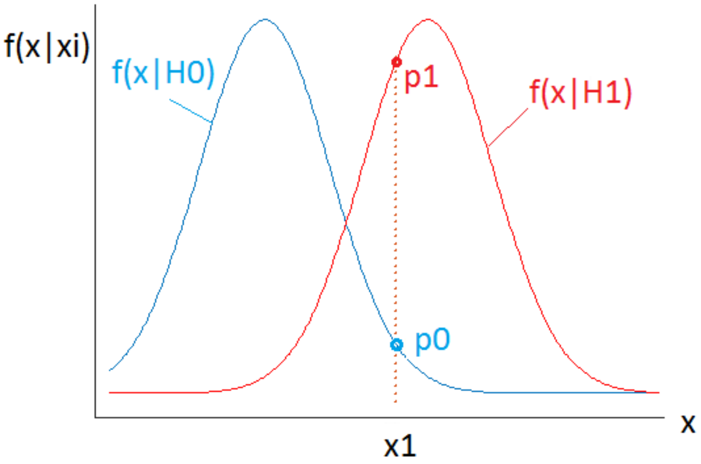

Figure 2.6: Maximum likelihood estimation

The mean and covariance are expected to be estimated from the HSI. The GLRT approach leads to many useful detectors in the form of:

$$D(x) \gtrless_{H_0}^{H_1} \eta \tag{2.13}$$

The LRT process is summarized in Figure 2.7: first, construct background and target hypothesis models; then, find the PDF of each model; and finally calculate the detection function for a specific pixel x based on the N-P criterion.

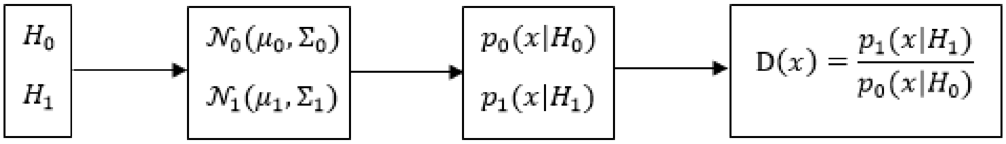

Figure 2.7: Development process for statistical detector

2.5 Evaluation methods

2.5.1 Receiver operating characteristic curve

There are two ways to define targets in an image: per pixel and per target [46]. This research focuses on a per pixel definition of targets. The per pixel definition of targets states that each pixel belongs to a target is treated as an individual target. Each target pixel inside the target regions is then considered as a candidate to be detected [10]. In order for an object to be perfectly identified as a target, each pixel in it must be classified as a target. An important part of a performance evaluation metric is the presence of a truth map for targets in question. A truth map contains, at minimum, the location of all target pixels in an image. In addition to the location, the type of target pixel may also be noted. A truth map can be used to differentiate between multiple targets as well as different backgrounds within an image.

The essential performance metric for a target detection algorithm is the Receiver Operating Characteristic (ROC) curve [38]. An ROC curve is the plot of the DR versus the FAR for a given target. ROC curves are generated based on the ground-truth information of the HSI. The ideal detector exhibits no overlap between H_0 and H_1 distributions and thus has detection the probability of 1 regardless of the FAR; the area under such a curve is 1 [47]. ROC curves can be stretched using a log FAR axis to visualize differences at low FAR values. A minimum FAR value must be set when using log ROC curves as the minimum cannot go to zero. The ROC curves provide a quantitative metric for performance comparison.

2.5.2 Separability analysis

The proposed method of this thesis uses the score of two popular detection algorithms, the MF and ACE, to construct a hybrid detection space (see Section 5.1 Hybrid detection space for details). In the experiments, pixel distribution in the hybrid detection space is used to show the separability between target and background. The hybrid detection space figure is shown in Figure 2.8: black dots are background pixels, while the red ones represent the targets. Ideally, they should not overlap, indicating that the targets are completely separable from the background [33]. This kind of graph can show how well a method differentiates the target from the background. A good detector would consistently suppress the background into a confined region while separating the targets [17].

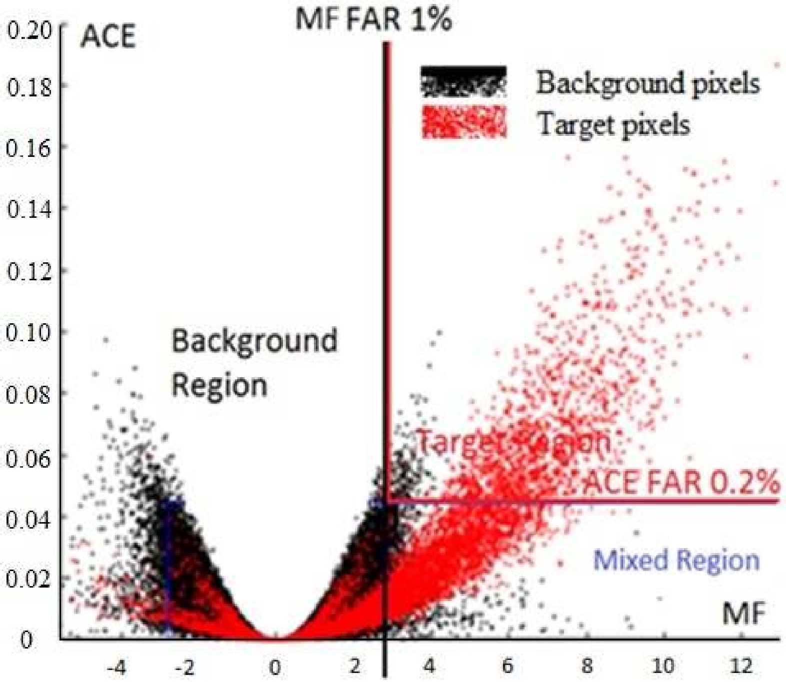

Figure 2.8: Hybrid Detection Space

3. TYPICAL PRE-PROCESSING ALGORITHMS FOR HSI

HSI processing algorithms can be classified as calibration, feature extraction, HU, abnormal detection, target detection, and classification for different application purposes. Because the data acquired from the sensor may vary due to the environmental interference, pre-processing techniques, such as calibration and band selection, are necessary in order to achieve high quality detection performance while using the traditional methods.

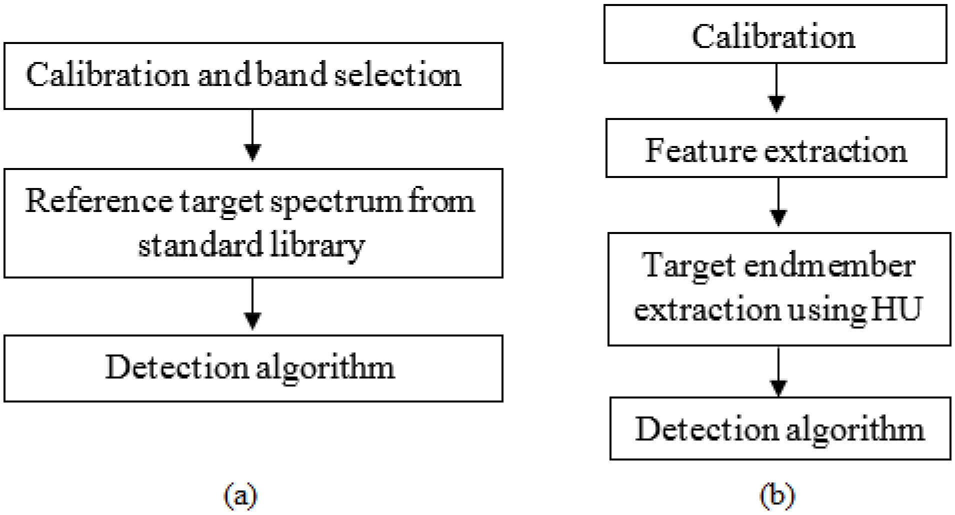

Figure 3.1: Flowchart of traditional detection methods

Traditional detection methods first acquire the HSI from the sensor, then convert the raw radioactive signals to reflectance signals and extract the main features from the data. For full pixel target detection, the SAM can be directly applied to compare the angle between the spectrum of the pixel under testing and the reference spectrum in standard library (Figure 3.1a). The reference target endmember spectra can also be extracted using HU to improve the accuracy. In some cases, the RXD can be applied before a detection algorithm to enhance the estimate of a background covariance matrix, which would be used in the detection algorithm (Figure 3.1b). All these pre-processing techniques are discussed in following.

3.1 Calibration algorithm

Radioactive signals of the HSI can be distorted by the atmospheric elements. Traditionally, to compare with the standard spectral library provided by authorized organizations, the signals acquired by the hyperspectral sensor must be calibrated to a usable format which has a similar unit with the standard spectra. The calibration step is essential to the overall performance of the hyperspectral system.

HSI calibration includes both spatial and spectral. In this thesis, the stress is spectral calibration. The raw data obtained from an imaging system consists of recorded radiance values reaching the sensor. However, this information does not easily relate to object information in the scene. The at-sensor radiance values are the results of atmospheric and illumination variables acting on the reflectance spectra of objects. Following are the two main steps for HSI calibration:

First, convert the raw sensor data to radiance which records the energy at a given time passing though the input aperture; second, convert the radioactive data to reflectance to reduce the impact of atmospheric interference and equipment noise. This process is also called atmospheric compensation. The difficulty in atmospheric compensation is how to estimate the distribution of atmospheric constituents such as, aerosols, vapor, etc.

There are various techniques for calibrating at-sensor radiance values to object reflectance values. The Empirical Line Method (ELM) is the most popular one [48]. The ELM works by associating pixels in a radiance image to known reflectance values. If no ground truth data is associated with the image, bright and dark pixels can be assigned approximate reflectance values. Ideally, full pixels for calibration should be located in a scene where reflectance measurements of the pixels have been made. In the ELM model, Radiance (*L*) and reflectance (*r*) would follow a linear relationship:

$$L = m \times r + b \tag{3.1}$$

where slope *m* is the atmospheric transmittance factor; offset *b* is the dark current offset. These terms are wavelength dependent but can be solved when good ground truth data is given. Then, the original image data can be converted to the reflectance unit.

3.2 Feature extraction and dimension reduction

The HSI contains a great amount of spectral information, which is very useful for target detection and classification. However, due to high spectral resolution of HSIs [36], there is huge redundant information between the adjacent bands; as well as some noisy channels and water absorption bands which are useless in detection applications. Furthermore, as there are so many bands in HSIs, huge amounts of calculation limit their applications. Hyperspectral dimension reduction keeps the original data information, and removes the noise and relevant information between bands. Therefore, dimensional reduction/band selection is important for HSI target detection and classification [49].

Principal Component Analysis (PCA) is the most basic hyperspectral dimension reduction technique [27]. The process of PCA dimensional reduction is as follows (Figure 3.2):

1. Vectorize the HSI information, input image represented as $X= (x_1, x_2, x_3, \ldots x_p)^T$, x_i is a $N*1$ column vector, here $N=m\times n$, means transforming an $m\times n$ size image into an $N\times 1$ column vector;
2. Centralize the data, each vector subtracts the mean column vector $E(x)$: $Y=X-E(X)$;
3. Solve for the covariance matrix $\sum$ for Y;

4. Solve for the characteristic matrix ***A*** for $\sum$;
5. Implement PCA transformation: $\Phi = A^T Y$.

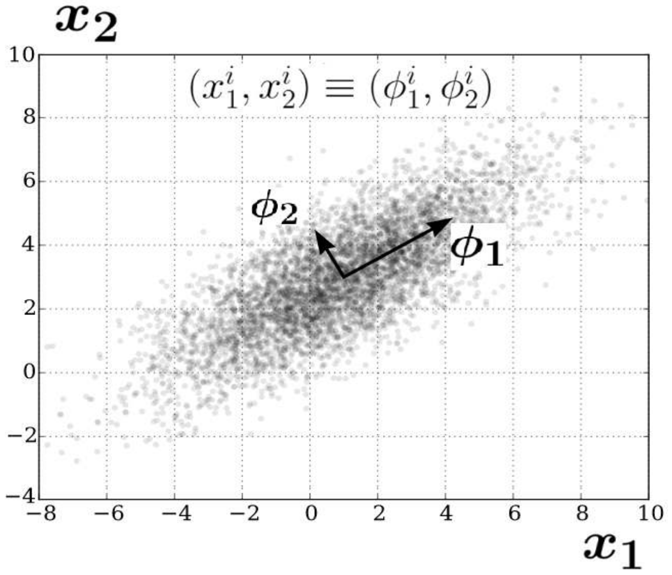

Figure 3.2: PCA Transformation, modified from [50]

PCA is a linear transformation, which has huge impacts on HSI data compression, noise removal, and feature extraction. After PCA processing, all the components are independent from each other. PCA can maximize the original data information while reducing the data dimensions.

An example of principal components of Moffett Field image used in Chapter VI is shown in Figure 3.3. It can be observed that, as the number of component increases, the eigen value decreases and the component image becomes noisy. The PCA algorithm can be applied to estimate the number of endmembers [51] and reduce the dimensions before HU. Moreover, it can also be a powerful tool to visualize the extracted main features of the high dimensional data.

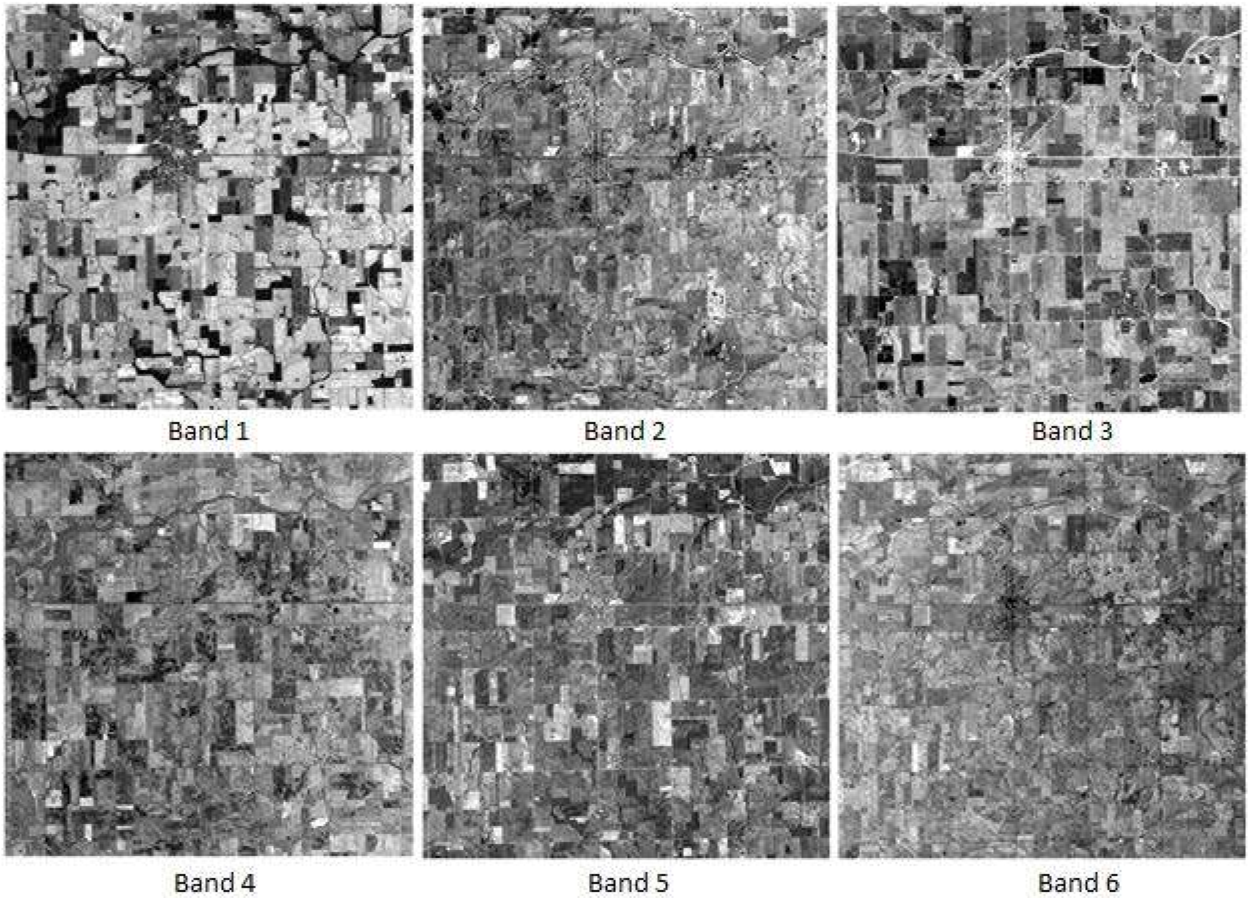
Band 1 Band 2 Band 3
Band 4 Band 5 Band 6

Figure 3.3: Sample PCA bands of Moffett Field image

3.3 Hyperspectral Unmixing (HU)

HU is the process of extracting the endmember of each material present in the scene. Observing from hyperspectral geometric characteristic, the HSI data has obvious CG structure which is based on the LMM. Normally, the closer the pixel to the vertex, the purer the pixel is. Unmixing algorithms based on the CG put more emphasis on the data structure for solving the endmembers in the original data distribution. The advantage of these algorithms is the simple model. Under the CG model, hyperspectral data has two constraints: non-negative and sum to one. The CG based HU is an elegant and efficient blind source separation approach.

Currently, endmember extraction algorithms that are under the CG model include: PPI, N-FINDR, vertex component analysis, etc. Basically, all these algorithms solve for the vertex points of the simplex, assuming that the pure pixels exist in the HSI. However, in real HSI, due to the atmospheric effects and remote distance, mixed pixels are more common than pure pixels, and this would lead to variation of spectra extracted from the scene and violation of the pure pixel assumption. Recent studies on blind HU have also introduced advanced techniques in optimal signal decomposition, such as Non-negative Matrix Factorization (NMF), dictionary-based sparse representation, etc.

This section introduces one basic HU algorithm: N-FINDR, which is based on the CG. The N-FINDR algorithm [5] looks for the endmembers of a dataset that maximize the volume of a simplex enclosing all image points in *N*-dimensional space. It operates under the assumption that pure endmembers or highly abundant mixed pixels exist in the space. The simplex enclosing all points with maximum volume has its vertices as the endmembers of the scene. The procedure of N-FINDR begins with a random initial selection of pixels (Figure 3.4a); then the volume of the simplex is calculated using following formula:

$$VE = \frac{1}{(N-1)!} abs(|E|) \tag{3.2}$$

where $E = \begin{bmatrix} 1 & 1 & \dots & 1 \\ e_1 & e_2 & \dots & e_N \end{bmatrix}$; $e_1, e_2 \dots e_N$ are the selected endmembers; N is the estimated number of endmembers; VE is the volume for the simplex. N-FINDR finds the maximum volume of the simplex by replacing the selected endmembers. The procedure repeats until there are no more endmember replacements (Figure 3.4 b).

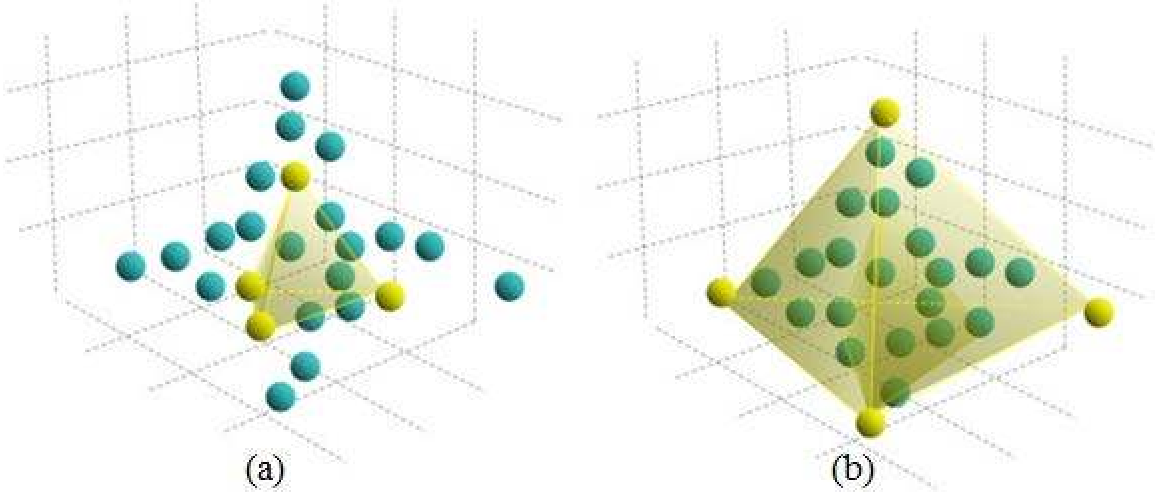

Figure 3.4: Graphical interpretation of the N-FINDR algorithm in a 3-dimensional space
(a) N-FINDR initial endmembers selection (p=4); (b) Final volume estimation by N-FINDR [52]

3.4 Abnormal detection

Abnormal detection is a scheme to detect pixels that obviously differ from the background. In spectral anomaly detection, pixels identified as anomalies should have significantly different spectral signatures [29, 30]. No prior knowledge of target spectra is needed in anomaly detection. The Reed-Xiaoli Detector (RXD) is one of the most popular methods for hyperspectral anomaly detection [53]. The RXD was developed to detect pixels with spectral characteristics other than background clusters with unknown spectra covariance. In the RXD, Mahalanobis distance between the global background and the pixel under testing is calculated based on the global covariance matrix.

Let H_1 be the target hypothesis and H_0 be the background hypothesis. The following are the statistical models for these two hypotheses [53]:

$$\begin{aligned} H_0 &: x = b \\ H_1 &: x = s + b \end{aligned} \tag{3.3}$$

where x is a sample pixel vector; s is the target signal; and b is the background cluster, which follows a MVN distribution with a mean vector μ, and a covariance matrix $\boldsymbol{C_b}$, i.e. $b \sim N(\mu, C_b)$. This leads to the background and target statistics: $x|H_0 \sim N(\mu, C_b)$ and $x|H_1 \sim N(\mu + s, C_b)$. With these definitions in mind, the PDF of $p(x|H_0)$ can be written as:

$$p(x|H_0) = \frac{1}{(2\pi)^{K/2}|C_b|^{1/2}} e^{-\frac{1}{2}(x-\mu)^T C_b^{-1}(x-\mu)} \tag{3.4}$$

where K is the number of bands in the HSI. $p(x_s|H_0)$ is assumed to be small for an anomalous pixel x_s, because it is expected to be far from the background. As $\frac{1}{(2\pi)^{K/2}|C_b|^{1/2}}$ is fixed, $(x - \mu)^T C_b^{-1}(x - \mu)$ should be larger for an anomalous pixel than that of the background.

In this expression, the background covariance matrix is known. In reality, the background covariance is unknown and can be estimated from a set of sample data, which affects the background statistics. Then, for a pixel $x = [x_1, x_2 \ldots x_K]^T$ with K bands, the output of RXD is:

$$RX(x) = (x - \hat{\mu}_b)^T \hat{C}_b^{-1}(x - \hat{\mu}_b) \tag{3.5}$$

where $\hat{\mu}_b$ is the estimated mean vector of the background and $\hat{C}_b$ is the estimated background covariance matrix. The RXD has been applied in many applications and is considered as the milestone of anomaly detection for hyperspectral data [29].

4. TARGET DETECTION ALGORITHMS

Remote target detection is a major application of HSI. It is widely utilized in the environment, urban, mineral and military fields. The HSI has high spectral and low spatial resolution. Targets more likely exist as subpixels in the HSI because of low spatial resolution. Therefore, the HSI target detection focuses on subpixel detection based on spectral variation, which is different from detection using the traditional high spatial resolution images.

Based on the data models theory, detection algorithms can be classified by subspace model, statistical model, and signal processing model. In this chapter, spectral angle mapper is introduced in Section 4.1, then some classical target detection algorithms based on the statistical model such as CEM, MF and ACE, are reviewed. Among them, the MF and ACE are applied in the proposed method in Chapter V.

4.1 Spectral angle mapper

The SAM, developed by Boardman [11], is a simple detection algorithm that computes the angle between two vectors. The SAM algorithm is expressed in a vector form as [54]:

$$D_{SAM}(x) = \frac{s^T x}{(s^T s)^{1/2}(x^T x)^{1/2}} \tag{4.1}$$

where *s* represents the target spectrum and *x* represents the pixel under test. This equation has values between 0 and 1 for a reflectance dataset. Similar pixels have a value near 1, which corresponds to a small angle between the vectors in question. Figure 4.1 shows a target vector and two pixel vectors. According to the SAM algorithm, pixel A is more likely to be the target than pixel B, due to the smaller angle between it and the target vector. The SAM is a quick and basic detection algorithm that is computationally inexpensive. However, the SAM is not good at subpixel target detection, as the abundances of some subpixel targets are too small to affect the angle. Furthermore, the SAM is dependent only on the spectral shapes of the objects and is independent of magnitude differences between the target and test pixel [55]. Illumination and shadow effects are eliminated, which creates difficulties when trying to discriminate between classes of similar spectral shape but different magnitudes. The SAM is included here as the baseline detection algorithm against which more elaborate algorithms are presented in following sections.

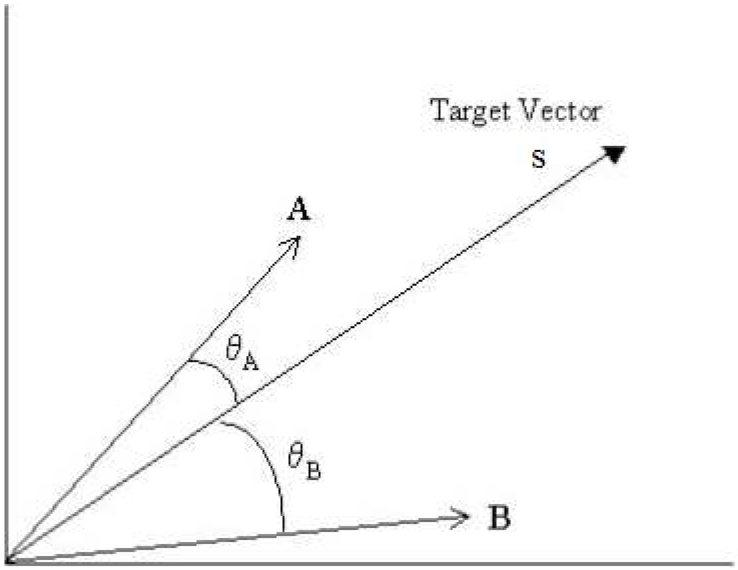

Figure 4.1: SAM angle comparison [46]

4.2 Constrained energy minimization

Constrained Energy Minimization (CEM) [30, 56, 57] is a statistically matched filter algorithm minimizing total energy *E* in the scene with a target constraint:

$$s^T w = \sum_{l=1}^{L} s_l w_l = 1 \tag{4.2}$$

where s is the desired signature; $w = (w_1, w_2 \ldots w_L)^T$ is the FIR linear filter with L filter coefficients. The FIR filter output y_i for a specific pixel r_i can be written as:

$$y_i = \sum_{l=1}^{L} w_l\, r_{il} = w^T r_i = r_i^T w \tag{4.3}$$

where $r_i = \{r_{i1}, r_{i2}, \ldots, r_{iL})^T$ for $1 \le i \le N$ is a sample input vector. Then, the total energy in the scene is calculated as:

$$E = \frac{1}{N}[\sum_{i=1}^{N} y_i^2] = \frac{1}{N}[\sum_{i=1}^{N} (r_i^T w)^T r_i^T w] = w^T \left(\frac{1}{N}\sum_{i=1}^{N} r_i r_i^T\right) w = w^T R w \tag{4.4}$$

where $R = \frac{1}{N}[\sum_{i=1}^{N} r_i r_i^T]$ is an $L \times L$ sample autocorrelation matrix of HSI dataset $S = \{r_1, r_2, \ldots r_N\}$. Minimizing (4.4) with the constraint $s^T w = \sum_{l=1}^{L} s_l w_l = 1$ yields:

$$\min_{w} \frac{1}{N}[\sum_{i=1}^{N} y_i^2] = \min_{w} w^T R w \ \textit{subject to} \ s^T w = 1 \tag{4.5}$$

The solution to Equation (4.5) can solve for the optimal weight vector w^*:

$$\mathrm{w} * = \frac{\mathrm{R}^{-1}\mathrm{s}}{\mathrm{s}^{\mathrm{T}}\mathrm{R}^{-1}\mathrm{s}} \tag{4.6}$$

Then, the CEM detector for a given pixel x can be represented as:

$$D_{CEM}(x) = w^{*T} x = (\frac{\mathrm{R}^{-1}\mathrm{s}}{\mathrm{s}^{\mathrm{T}}\mathrm{R}^{-1}\mathrm{s}})^T x = \frac{\mathrm{s}^{\mathrm{T}}\mathrm{R}^{-1}\mathrm{x}}{\mathrm{s}^{\mathrm{T}}\mathrm{R}^{-1}\mathrm{s}} \tag{4.7}$$

4.3 Matched Filter (MF)

The MF and Adaptive Coherence/Cosine Estimator (ACE) are two hypothesis-test-based detection algorithms. The MF and ACE first formulate the target detection as binary hypothesis test problems and then use the LRT or GLRT to obtain the detectors [58]. These algorithms are statistical in nature, and are based on signal models, where a data vector x conditional to the background (H_0) hypothesis is assumed to follow a MVN distribution [47]. The inverse covariance matrix of the background data is used to find new coordinate axes, where the background follows spherical or "whitened" distribution. Most multivariate detection algorithms are simple tests of Euclidean geometry in the whitened space.

After subtracting the mean value from the original background data, the hypothesis model for MF [38, 59] is:

$$\begin{aligned} H_0 &: x = n, \\ H_1 &: x = as + n, \end{aligned} \tag{4.8}$$

The MF model is based on the assumption that the background noise has a Gaussian distribution $N(0, C_b)$, and the target also follows a Gaussian distribution, $N(as, C_b)$, which have the same covariance statistics, but a different mean. a is an average target abundance value, $s = [s_1 s_2 \ldots s_p]^T$ is the target spectral signature. For a p×1 input x with distribution:

$$x \sim N_p(as, \sigma_b^2 C_b)$$

where $a \geq 0$ and $\sigma_b^2 \geq 0$ are scalar quantities; s is a p×1 known vector; and $\boldsymbol{C_b}$ is a $p \times p$ positive definite known matrix. Since the matrix $\boldsymbol{C_b}$ is positive definite, its square-root decomposition $\boldsymbol{C_b^{1/2}}$ is invertible. Therefore, the whitening transformation is [38]:

$$\tilde{x} = C_b^{-1/2} x, \tilde{s} = C_b^{-1/2} s \tag{4.9}$$

resulting in a new distribution:

$$\tilde{x} \sim N_p(a\tilde{s}, I)$$

which is spherical ("white") normal distribution, and the detection problem is equivalent to the original one, but the new distribution can simplify derivation and analysis. The LRT for the whitening model leads to the following result [38]:

$$y_1 = a\tilde{s}^T\tilde{x} \gtrless_{H_0}^{H_1} \eta \tag{4.10}$$

where *a* is the unknown target abundance (*a* = 0 when no target is present and *a*>0 when a target is present); *n* is zero-mean Gaussian random background noise. Since *a*>0 for the H_1 hypothesis, both sides of the inequality can be divided by *a*. The resulting equation,

$$y_2 = \tilde{s}^T\tilde{x} \tag{4.11}$$

is independent of *a*. However, the MF does not have the Constant False Alarm Rate (CFAR) property because the threshold depends on *a*.

Equation (4.11) is often divided by $\sqrt{\tilde{s}^T\tilde{s}}$, which is the magnitude of the target vector in the whitened space. Since this value is constant, the division does not impact the performance, and the output of the MF for input x is [29]:

$$D_{MF}(x) = \frac{\tilde{s}^T\tilde{x}}{\sqrt{\tilde{s}^T\tilde{s}}} = \frac{s^T\hat{C}_b^{-1}x}{\sqrt{s^T\hat{C}_b^{-1}s}} \gtrless_{H_0}^{H_1} \eta_{MF} \tag{4.12}$$

where $\hat{\boldsymbol{C}}_{\boldsymbol{b}}$ represents the estimated covariance matrix for the centered observation data and η_{MF} represents a threshold. D_{MF} is the projection length of the test vector onto the target vector in the whitened space. If the projection length is greater than what is typical of the background, the H_0 hypothesis is rejected and the test vector is determined to contain the target [47].

The MF detector has a very similar form to the CEM detector. The major difference is whether the mean vector is removed from all the data pixels in advance. Geng showed theoretically that the CEM detector will never improve over the MF [60]. That is to say, of these two benchmark target detection methods, the CEM can now be considered obsolete.

4.4 Adaptive Coherence/Cosine Estimator

In practice of MF, a and $\sigma_b^2$are unknown. However, they can be estimated using Maximum Likelihood Estimates (MLEs) [38]:

$$\begin{gathered} \hat{a} = \frac{\tilde{s}^T\tilde{x}}{\tilde{s}^T\tilde{s}}, \\ p\hat{\sigma}_b^2 = \tilde{x}^T\tilde{x} - \frac{(\tilde{s}^T\tilde{x})^2}{\tilde{s}^T\tilde{s}} \end{gathered} \tag{4.13}$$

The resulting maximum likelihood function is $exp\left(-\frac{p}{2}\right)/(2\pi\sigma_b^2)^{\frac{p}{2}}$ and can be rewritten as [37]:

$$\Lambda_G(\tilde{x}) = (\frac{\hat{\sigma}_b^2\ under\ H_1}{\hat{\sigma}_b^2\ under\ H_0})^{-p/2} = [1 - \frac{(\tilde{s}^T\tilde{x})^2}{(\tilde{s}^T\tilde{s})(\tilde{x}^T\tilde{x})}]^{-p/2} \tag{4.14}$$

Since a>0 under H1 and only the term $\tilde{s}^T\tilde{x}$ retains the sign of $\hat{a}$, the Normalized MF (NMF) is defined by:

$$y_{NMF} = \frac{\tilde{s}^T\tilde{x}}{\sqrt{(\tilde{s}^T\tilde{s})(\tilde{x}^T\tilde{x})}} = \frac{s^T C_b^{-1} x}{\sqrt{s^T C_b^{-1} s}\sqrt{x^T C_b^{-1} x}} \gtrless_{H_0}^{H_1} \eta_{NMF} \tag{4.15}$$

where the covariance matrix $\boldsymbol{C_b}$ is estimated from the data. y_{NMF}^2 is also known as the Adaptive Coherence/Cosine Estimator (ACE).

After the whitening transformation, the estimated covariance matrix of whitened hyperspectral background data equals the identity matrix [29]. An intuitive geometrical description of the MF and ACE detectors in the whitened space are provided in Figure 4.2 [38]. The vector $\tilde{s}/||\tilde{s}||$, where ||▪|| denotes Euclidean distance, is a unit vector. y_{MF} is the projection distance of the observation vector onto the target. In contrast, the value of y_{NMF} is the cosine of the angle between the observation and target vector. Therefore, the ACE is invariant to scaling of the target and observation measurements. The essence of target detection process is to test any pixel in the image to find out whether it belongs to H_0 or H_1 [61]. The ACE detector is used in this way to discriminate between object signatures. It is assumed that only one kind of target presents in the scene and all the mixture targets lie in the vector which connects the background and the target signature. The ACE is a measurement of how a pixel fits the mixing model, while the MF is defined as the target fill fraction of a pixel.

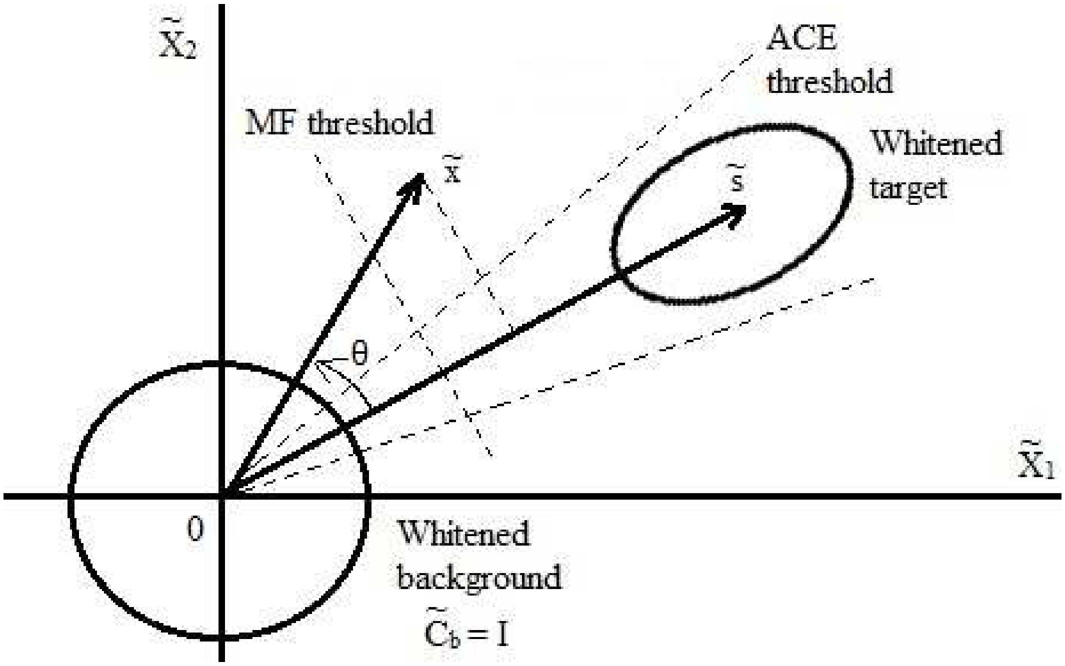

Figure 4.2: Geometrical description of the MF and ACE detectors in whitened space

A 2001 study [62] by Manolakis showed the ACE algorithm generally performs better than all other MF detection algorithms examined and is therefore adopted in the proposed method.

The whitened data is assumed to follow a spherical normal distribution in MF and ACE derivations. However, in real practice, the whitened data are not white. Therefore, further study about the interband and intra/interband correlation of noise can improve the noise covariance estimation and improve the detection performance. A comparison of basic detection algorithms is shown in Table 4.1.

Table 4.1: Comparison of basic detection algorithms

Detection algorithm	H1	H0	Detector	Year/ Reference
RXD	$x = s + b$ $N(\mu+s,C_b)$	$x = b$ $N(\mu,C_b)$	$RXD(x) = (x - \hat{\mu}_b)^T \hat{C}_b^{-1}(x - \hat{\mu}_b)$	1990/[7]
SAM	Not applicable		$D_{SAM}(x) = \frac{s^T x}{(s^T s)^{1/2}(x^T x)^{1/2}}$	1993/[11]
CEM	Not applicable		$D_{CEM} = \frac{s^T R^{-1} x}{s^T R^{-1} s}$	1993/[57]
OSP	$x = s\alpha_t + B\beta + n$	$x = B\beta + n$	$D_{OSP} = s^T P_b^{\perp} x$	1994/[18]
MF	$x = as + n$ N(as Cb) $N_p(a\tilde{s}, I)$	$x = n$ N(0 Cb) $N_p(0, I)$	$D_{MF}(x) = \frac{s^T \hat{C}_b^{-1} x}{\sqrt{s^T \hat{C}_b^{-1} s}}$	1992/[13]
ACE	$x = as + n$ N(as Cb) $N_p(a\tilde{s}, I)$	$x = n$ N(0 Cb) $N_p(0, I)$	$D_{ACE}(x) = \frac{(s^T \hat{C}_b^{-1} x)^2}{(s^T \hat{C}_b^{-1} s)(x \hat{C}_b^{-1} x)}$	1995[14]

5. PROPOSED METHOD

As discussed in Chapter III, traditional material detection follows steps of calibration, feature extraction and comparison with the standard spectral library using detection algorithms. The performance of traditional HSI target detection can be easily affected by the following factors:

- Errors between the reference spectrum in library and image spectra
- Uncertainty of material spectra due to illumination, atmosphere, background environment and equipment noise
- Calibration and pre-processing errors
- Inaccurate background/noise modeling

Therefore, this kind of method may not detect subpixel targets very well and it is necessary to improve HSI detection algorithms. For target detection purposes, the HSI pixels can generally be divided as target and background. Improving the representation of target and background can lead to better separation of target and background. Therefore, addressing target variation and better estimating background are two major challenges in improving subpixel target detection. Finding methods that can suppress the background and stress the majority of targets can improve the detection performance greatly.

In the traditional statistical detection method, it is not appropriate to use any random pixel containing the target as the target signature because it would be corrupted by the background [17]. Furthermore, using the target signature from the scene would also reduce the pool of targets and bias the results. Therefore, most of the current methods use atmospheric compensation and HU techniques to extract the target spectrum from the image. Subspace methods, such as MSD and ASD, require the description of the target and background using many endmembers. Since the endmembers are unknown while testing a randomly selected dataset, HU technology such as N-FINDR and PPI, is needed to extract the endmembers. However, HU requires the estimation of the number of endmembers and would lead to inaccurate results in the case of lacking full pixel endmembers in the scene. Although recent research [21, 23] shows representation methods can achieve higher detection performance than statistical and subspace methods, they also highly rely on the dictionary sample size and the constraints of contexture pixels to improve the performance. Library construction, computation cost, and constraint design are the main concerns for these methods. Table 5.1 shows the comparison of these three categories of detection methods.

Table 5.1: Comparison of three categories detection methods

Detection Method	Advantages	Limitations	Possible improvement methods
Statistics [13, 14]	a. Easy implementation b. Intuitive physical meaning	a. Based on MVN assumption b. Relies on reference target spectrum	a. Target free background estimation b. Improve the reference target spectrum c. Kernel transformation d. Locality constraints
Subspace [15, 18]	a. adapt to spectral variation better than single target spectrum	a. Require all endmember of background and target b. Sensitive to noise	a. Improve endmember extraction

Representation [21, 23]	a. High accuracy with over complete dictionary and proper constraints b. Good for some special target spectra	a. Over complete dictionary required b. Regularization and contextual constraint required c. Calculation complexity	a. Fusion with statistical method

As HSI applications become more and more common, future target detection algorithms should depend less on a standard library, be adaptive to spectral variation and most importantly, provide high detection performance without any specific constraint on a specific case.

A good target detection algorithm can differentiate a target from the background cluster. Reference target spectrum and background representation are two critical variables in target detection algorithms and affect the performance greatly. Therefore, extracting a better representation of the target and the background is essential in subpixel target detection. Although larger target samples are needed to achieve accurate detection performance, in most cases, only a few target samples are available [10]. This chapter introduces a new method, which starts with a few randomly picked target spectra, and then improves the reference target spectrum iteratively using hybrid detection space to address the aforementioned challenges and gradually improve the target detection performance. The ACE is used to estimate the target with minimum interference from the background and the MF is used to estimate the background with minimum interference from the target.

5.1 Hybrid detection space

The proposed method is based on the hybrid detection space (Figure 2.7), which is constructed by scores of the MF (x axis) and ACE (y axis). The MF and ACE are two popular target detection algorithms based on statistical theory. The MF has the physical meaning of projection length of data vector onto the target vector, while the ACE means the square of cosine of the spectral angle between the test pixel's spectrum and the target's spectrum in the whitened space (Figure 4.2).

The whitened background is assumed to follow a sphere normal distribution $N_p(0, I)$, in an N dimensional space. If N is fixed, for a constant FAR, the detection angle for the ACE is fixed, and the ACE score is also fixed. This is the same for MF. Geng proved that adding any band linearly independent of the original ones improves the detection performance of the CEM [63]. Experiments show the same results for both the MF and ACE. The more bands, the lower the scores are for background's ACE. If the background covariance matrix is estimated accurately, with a constant FAR, then the ACE and MF scores are fixed. For example, for a HSI of 172 bands, the ACE score is approximately 0.06 at 0.2% FAR, and the MF score is approximately 2.7 at 1% FAR. This means most of the background would be confined to a small background region in the hybrid detection space.

The hybrid detection space transforms the high dimensional whitened data to a visual form using the distance and angle, which are basic elements in geometry. High abundance targets are far from the background region. The corresponding position in the hybrid detection space for a certain pixel can be used to determine whether it is the target, which helps in analyzing the data and separating the target from the background.

As the whitened background follows the sphere normal distribution $N(0,I)$ in high dimensional space, the center of the hypersphere with the highest distribution density is transformed to the origin of the hybrid detection space, and the background distribution in the hybrid detection space is symmetrical about the *y*-axis. If there are some targets present, the pixel distribution in the hybrid detection space performs as asymmetrical about the *y*-axis. As targets would trend towards the target center, which is in the first quadrant, targets would probably fall in the first quadrant and the pixels in the second quadrant could be considered as pure background. The overall FAR can be estimated by observing the FAR of background distribution in the second quadrant. This helps in setting thresholds for separating the target and background.

5.2 Low abundance target detection

The detection performance for subpixel targets can be affected by the following factors:

- Distance between the centers of target and background
- Bands and abundance of subpixel targets
- Detection algorithms

As the whitened background follows the sphere normal distribution, the whitened hypersphere is defined with a radius equal to the distance from the center of the background to the hyperplane, which divides the background into 99% and 1%. In most real aerial HSIs, targets with an abundance of greater than 50% are usually fewer than targets with abundance lower than 50%. To evaluate the proposed method more accurately, subpixel targets within the whitened hypersphere are defined as low abundance targets and those outside the hypersphere are defined as high abundance targets. Specifically, FARs greater than 1% are called high FARs and less than 0.1% are low FARs. Normally, low abundance targets would have an abundance less than 10% and high abundance targets would have an abundance greater than 10%.

High abundance targets fall outside the hypersphere and most likely fall inside the hypercone with a small detection angle. That is to say, both the MF and ACE methods have excellent detection performance on high abundance targets. However, low abundance targets are more likely mixed with the background and hard to detect. For low abundance targets with fill fractions less than 1%, the targets are likely to fall near the center of the background and are extremely difficult to differentiate from the background. As the energy of these targets is so small, these targets can be considered as background in order to simplify the detection process.

The proposed method aims to improve the detection performance for Low Abundance Targets with abundance value ranging from 1%- 10%, which are noted as LATs. If one method can work well on LATs, it should work well for high abundance targets, and improving the overall detection performance.

As shown in Figure 5.1, for the MF method , LATs trend towards the center of target from the center of the background; thus at a high FAR, most of LATs can be detected, as indicated to the right of the vertical line FG. However, at a low FAR, the detection performance is poor because most of the LATs are within the radius of the hypersphere and mixed with the background. As both the target and the background are assumed to follow an MVN distribution, for a constant abundance "a", the subpixel targets would also follow an MVN distribution. If "a" varies from 0 to 1, the resulting target distribution would be greater along the horizontal line, BT. In low FARs, the ACE can still capture some of the targets between the center of the background and the reference target spectrum (Area DBE), thus, it has better performance than that of the MF. As the FAR increases, the detection angle also increases, however, there are still some LATs still fall outside the hypercone area ABC in the figure.

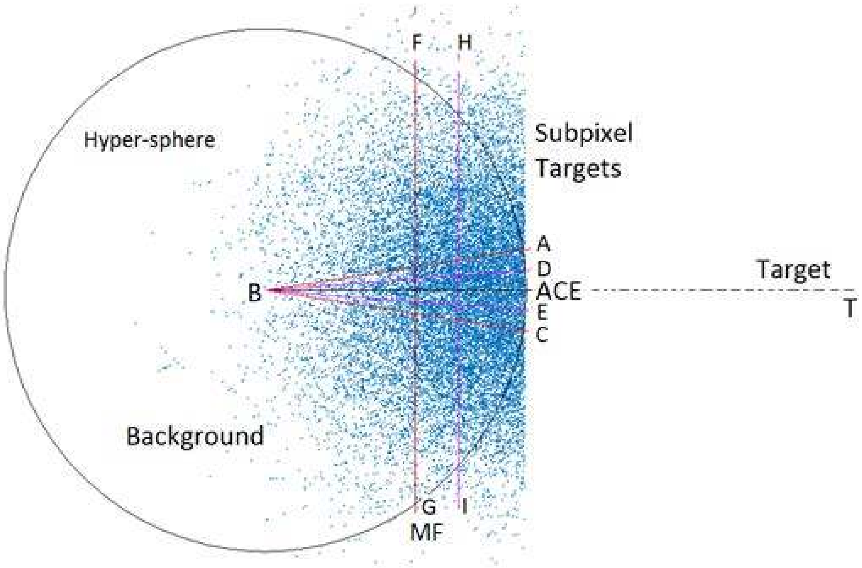

Figure 5.1: Subpixel target detection inside hypersphere.

Blue points are low abundance subpixel targets. Back circle is the hypersphere in two-dimensional space. Region ABC and line FG are the decision cone/plane at a high FAR for ACE and MF algorithm, respectively. DBE and HI are the decision cone/plane at a low FAR for ACE and MF algorithm, respectively.

Therefore, for LATs, the ACE has better performance at low FARs and the MF has better performance at high FARs. Because of the properties of these two algorithms, the ACE is good for capturing potentially pure target pixels from the scene and the MF is good for extracting potentially pure backgrounds.

5.3 MF background estimation

For both the MF and ACE, it is assumed that the background and target follow an MVN distribution. The background covariance matrix is essential in estimating the PDF of the background and target, and ultimately affects the detection results. Conventional background models seem to be effective; however, they cannot adapt to the diversity of the real world. When the background pixels are contaminated by target signals, the estimated background would strongly deviate from the real background distribution and lead to corruption of the estimated statistics [31]. Background contamination with target signals violates the pure background assumption and has a deleterious effect on target detection. Therefore, the development of complex models for background estimation is necessary as the background is indeed complex [31]. A target-free background model could improve detectability of subpixel targets.

It is impossible to find a perfect model that can capture all the characteristics of hyperspectral background [38] because the presence of some man-made objects can produce anomalies that cannot be predicted by any model. However, it is useful to obtain a relative effective model by excluding the majority of target pixels while estimating the background. Many methods have been developed for excluding the targets from the background to achieve greater multivariate normality.

A. Adaptive threshold

As background signals may vary from location to location, one way to counteract this phenomenon is to use adaptive threshold technique [33]: setting appropriate thresholds for different regions can better characterize the background and exclude the target signals.

B. HSI pre-clustering

Pre-clustering using HSI classification can improve the target detection performance. Data distribution within one class is more likely to follow the MVN distribution than inter-class mixtures. Therefore, the estimated statistics can better suppress the background and reduce the FAR. However, the inclusion of target pixels in the background is a problem while performing the HSI classification [64].

C. Mahalanobis Distance

To find the background and abnormality, it is necessary to calculate the Mahalanobis Distance (RXD value):

$$MD(x) = \sqrt{(x - \hat{\mu})^T \hat{C}_b^{-1} (x - \hat{\mu})} \tag{5.1}$$

Any pixel with a score greater than a certain threshold (i.e., above the red line in Figure 5.2) is considered to be an outlier. Otherwise, pixels under the red line in Figure 5.2 are considered as background.

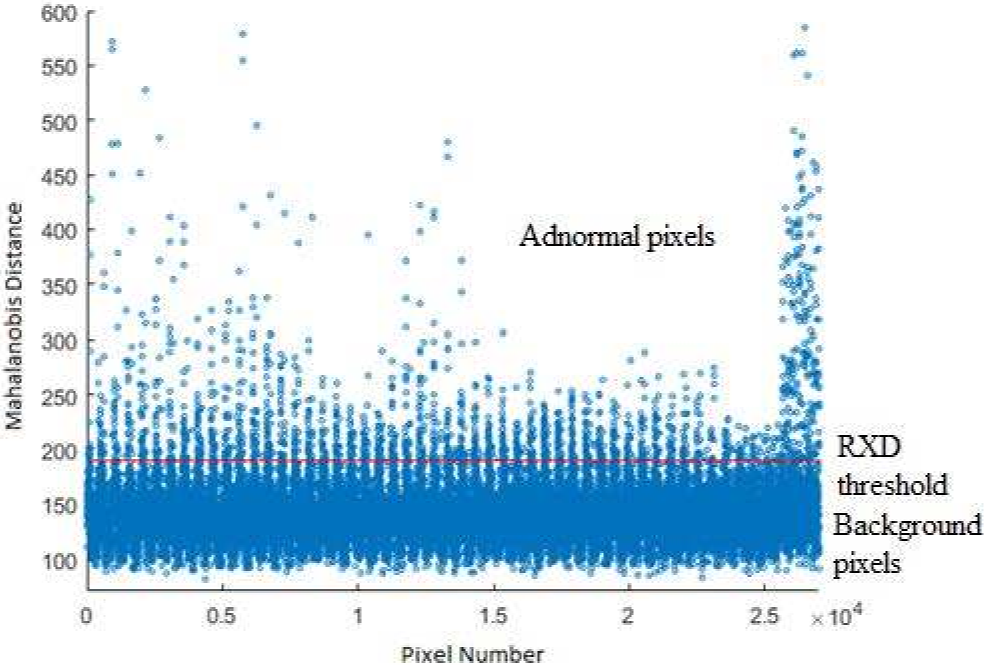

Figure 5.2: RXD background estimation

The claimed background may actually contain LATs while using the Mahalanobis method because the signals of LATs are too small to be present as abnormalities (Figure 5.3a). This usually results in an ill-form of the covariance matrix and affects the detection performance. The proposed method attempts to remove more LATs in the background region while estimating the background.

The global covariance matrix without excluding all targets is inaccurate as the estimated background center moves towards the targets. This would lead to errors in estimating the PDF of background. Generally, the MF algorithm has good detection performance at a high FAR, therefore, it can exclude most of the targets from the background (Figure 5.3b). In the hybrid detection space, the area with MF FARs greater than 1% is considered as background region. As the remaining targets only have small fractions or of low intensity, it is assumed that the background is close to being a target-free background. This generates a covariance matrix close to the real one, achieves accurate PDF for the background and improves the detection performance.

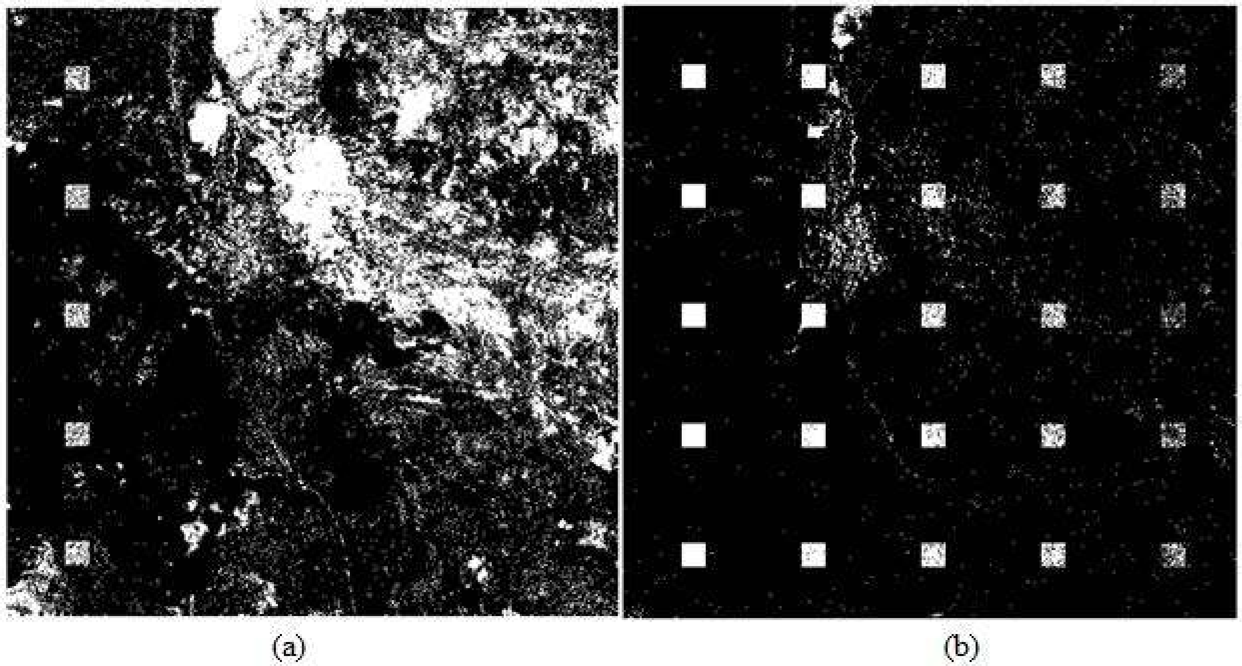
(a) (b)

Figure 5.3: Background estimation using (a) the RXD method compared to (b) the MF method

Another purpose of the MF background covariance matrix evaluation is to keep the background as the background during the iterative process. As most of the background (99%) is located inside the background region, the corresponding covariance matrix reflects the relationship between bands and constrains the background pixels into a small area, with low scores when using both the MF and ACE. Then, the background probably stays in or near the background region of the hybrid detection space.

5.4 Hybrid detection algorithm

The proposed hybrid detection algorithm is as follows:

Algorithm 1: Hybrid detection algorithm

```
Initialization:
    1. Pick one to five high abundance target pixel(s) from the image, and average them to get an initial reference target spectrum
    2. Perform the MF and ACE detection algorithms using the initial target spectrum and global covariance matrix
Main iteration:
    3. Consider all the pixels with ACE FARs less than 0.2% (0.01% for the first and second iterations) and MF FARs less than 1% as targets
    4. Average the targets to update the reference target spectrum $sp(i)$
    5. Use the region with MF FARs greater than 1%, assumed to be the background, in order to calculate the respective covariance matrix $\boldsymbol{C_b(i)}$
    6. Use the new reference target spectrum $sp(i)$ and the background covariance matrix $\boldsymbol{C_b(i)}$ to perform the MF and ACE algorithms
    7. Calculate the evaluation metrics: $N_i$ and $L_i$
Stop the main iteration if $N_i/N_{i-1}<1.02$ or $L_i/L_{i-1}<1.02$
else go to Step 3
```

8. Follow the detection order from the high ACE score to the low ACE score in the target and mixed region first, then from the high MF score to the low MF score in the background region

The traditional method obtains the reference target spectrum from the standard library or extracts it from HSI using HU. The reference spectrum from the standard library may not identify or be close to that of the actual target being sought due to spectral variation. Therefore, it would be inaccurate to use the standard one. Another concern is the original data also need to be calibrated before applying the detection algorithm. Furthermore, because the HSI covers a wide range, there is not a uniform parameter that generally applies to all bands and locations in the calibration model. Therefore, errors always happen in calibration.

On the other hand, extracting the target spectra from the scene using HU based on the CG seems to be a better solution. However, a mismatch in estimating the number of endmembers or lack of full pixels produces inaccurate results. Computational complexity is also a concern. In this section, a new method is introduced to extract the reference target spectrum from the HSI using iterative improvement.

In HSI, both the background and the target are assumed to follow the MVN distribution and subpixel targets are linear combinations of background and target subsets. Therefore, the subpixel targets would also follow MVN distribution and have greater density along the line BT, which connects the centers of background and target (Figure 5.4).

The background is always constrained in the background region while using the MF background covariance matrix evaluation. Whitened background would follow hyper-sphere normal distribution and the detection angle for the hypercone would be the same for a constant FAR. To achieve better detection performance, the reference target spectrum must be close to line

BT so that the detection region can cover more targets. However, for a randomly picked spectrum, it may fall far away from line BT, for example, *sp1*. As a result, the detection area can only cover a region (ABC) with low density target distribution.

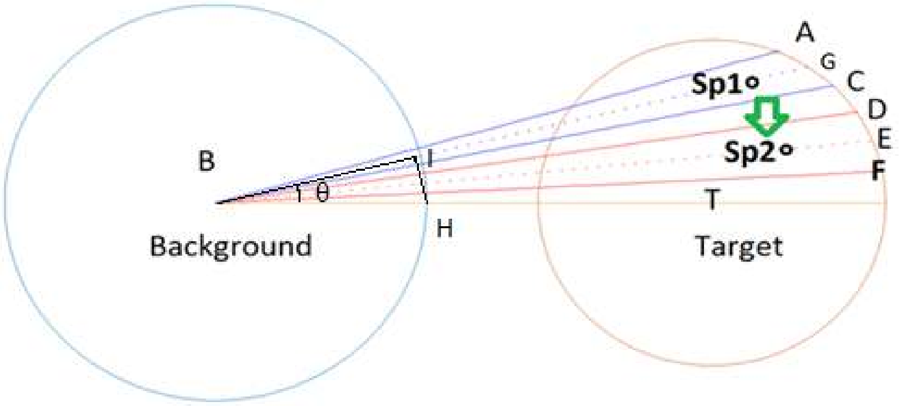

Figure 5.4: Terminal condition I: maximum target coverage

In the hybrid algorithm, first, the target dictionary is assumed to be unknown. One or a few high abundance target pixel(s) are randomly picked from the image and averaged to get the initial reference target spectrum. Then, the MF and ACE detection algorithms are applied to the data using a global covariance matrix. In the hybrid detection space, the corresponding threshold value for a certain FAR can be estimated by observing the pixel distribution in the second quadrant (Figure 5.5). The region with MF FARs greater than 1% is considered as background (left side of black line); the region with ACE FARs lower than 0.2% and MF FARs lower than 1% (upper right corner of the red curve) is considered as the target region (setting ACE FARs 0.01% for the first two iterations, because the target subset is very small at the beginning, high FARs brings more background pixels into the target subset and reduces the accuracy of detection). The region in the lower right corner is defined as mixed region.

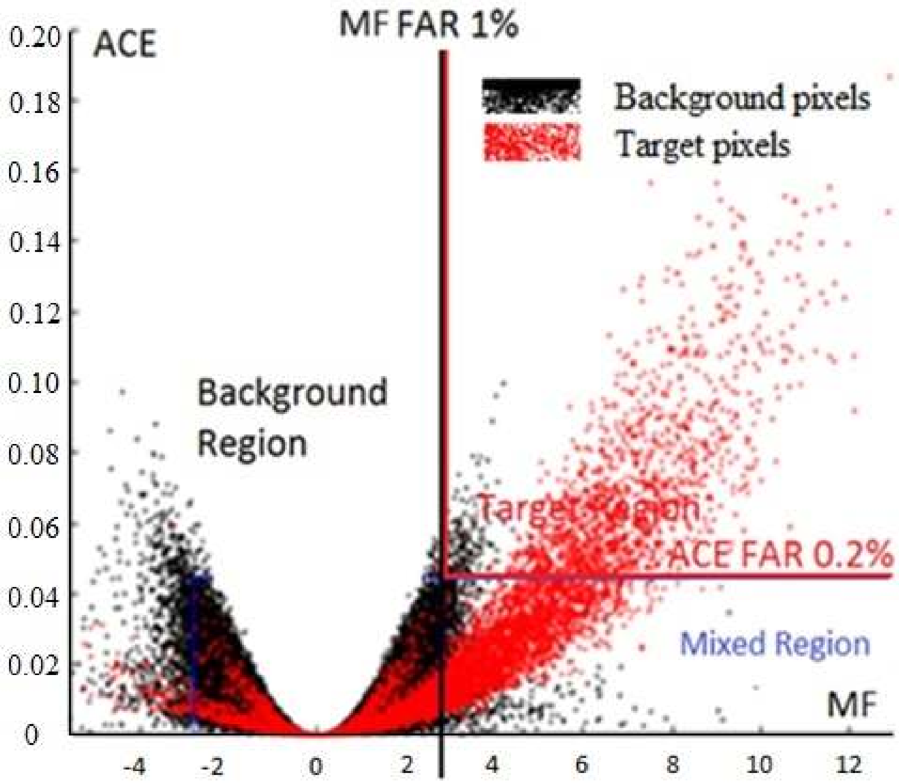

Figure 5.5: Hybrid detection space

Then, a new background covariance matrix is evaluated from the new background subset and a new reference target spectrum for the next iteration is calculated by averaging all the pixels in the target region. If the target spectrum is obviously different from those of the background clusters, the target and background distributions are shown in Figure 5.4. In the detection region ABC, because region GBC is closer to the line BT than region ABG, the target distribution should be higher in region GBC. As a result, the new reference target spectrum, for example- *sp2*, which is the average spectrum of target samples in the target region- would be closer to the line BT than *sp1* would be. When applying *sp2* as the reference target spectrum with the same detection angle, more target pixels that are close to the line BT can be detected. Then, most of the targets would have higher ACE and MF scores, and thus would escape from the background region. For example, if point H in line BT is the pixel to be tested, then as the reference target spectrum moves from *sp1* to T, the ACE score increase from $\cos(\theta)$ to 1, and point H escapes from the background region. Then, the new background is purer than the previous one. After some iterations, the reference target spectrum falls on or very close to line BT. Then, the number of pixels covered by the hypercone outside the hypersphere, N_i (where i is the number of iteration)- which includes the detected targets and some constant false alarms of the background- would reach a maximum value, and the iterative process should be terminated.

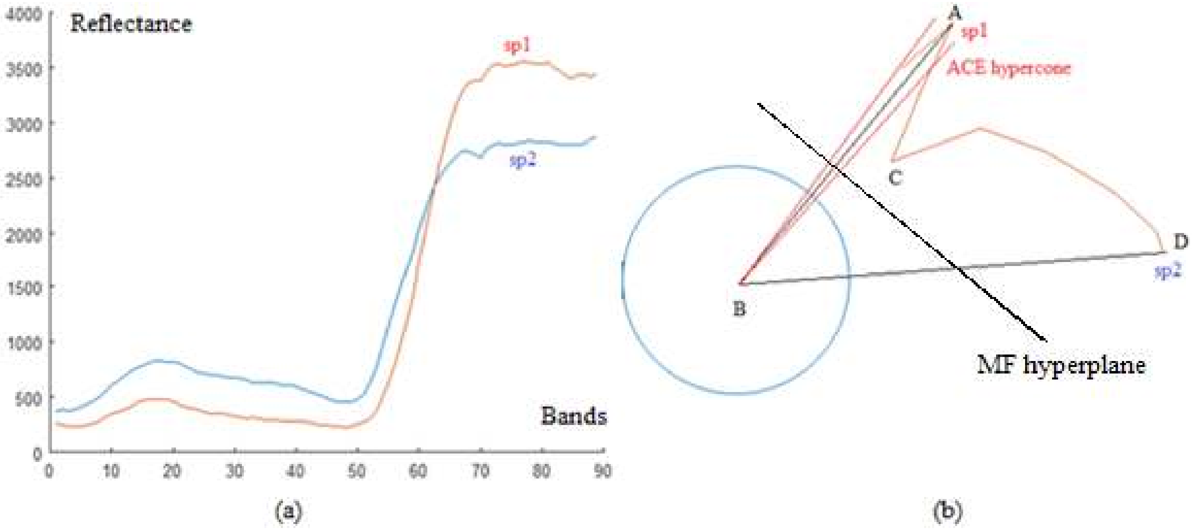

Figure 5.6: Abnormalities with similar spectrum to target present

(a) Target spectrum *sp1* and similar abnormity spectrum *sp2*; (b) targets, similar abnormalities and background distribution in the whitened space

Although both the MF and ACE can be used for iterative improvement of the target spectrum, the ACE can capture more LATs in low FARs, thus providing more information about target distribution. Furthermore, if some abnormalities (*sp2*) with similar spectra as the target (*sp1*) are present in the scene, as shown in Figure 5.6, since the decision hyperplane of the MF divides the space into two parts, then the resulting targets are contaminated by the other abnormalities, thus affecting the final detection performance. On the other hand, the hypercone of ACE only covers 1/500 of the space while using 0.2% FAR; 500 is a number that is much higher than the number of endmembers existing in the scene, so, the overlap probability of target and other abnormalities should be much lower than when using MF. This would ensure the purity of the target samples; therefore, the ACE is selected to estimate the target samples.

If abnormalities similar to the target are present in the scene, then the iterative process may deviate from the target spectrum to other abnormalities; because the transition region may also have a higher pixel density than the actual target region. A new metric, maximum MF score (Figure 5.7), is needed to improve the accuracy of the proposed method.

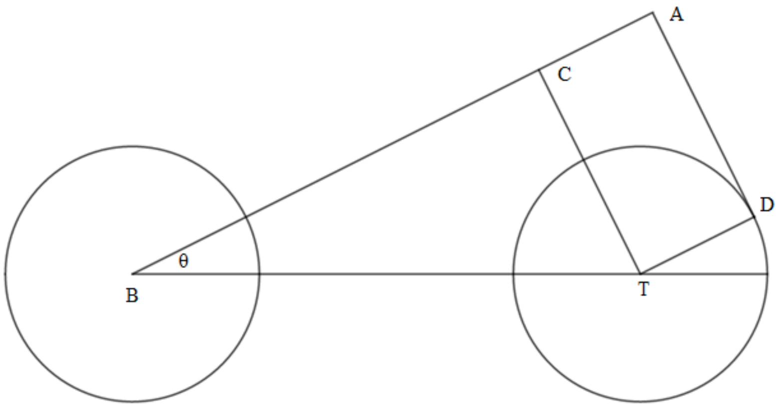

Figure 5.7: Terminal condition II: maximum MF score

In Figure 5.7, the points B and T are the centers of the background and target, respectively, and A is the reference target spectrum. The maximum MF score is the distance of AB:

$$Max(MF) = AB = BC + CA = BT \times \cos(\theta) + R_T \tag{5.2}$$

where BT is the distance from T to B; θ is the angle between the reference target spectrum and the central line; R_T is the radius of targets in whitened space. Since BT and R_T are constant, the maximum MF score increases as θ decreases. The MF score reaches a maximum value when the reference spectrum is very close to the central line. As in the transition region, the maximum MF score usually decreases; this can imply that the spectrum is moving to an abnormal region. To mitigate the effect of abnormal distribution, the top 100 MF scores are averaged as an index (denoted as L_i for *ith* iteration) to determine whether the iterative process should be terminated.

In sum, by ignoring minor errors in the iterative process, the terminal conditions for the iterative process are set as: $N_{i+1}/N_i<1.02$ or $L_{i+1}/L_i<1.02$. The iterative process should be terminated if either condition is satisfied; and the optimal spectrum is assumed to be achieved.

Generally speaking, the MF has better performance at high FARs while the ACE has better performance at low FARs. In the hybrid detection space, the background region has the lowest Target to Background Ratio (TBR) and the target region has the highest TBR. Therefore, avoiding the background region yields better detection performance while keeping a constant FAR. During the detection process, the detection order first should be from the high ACE score to the low ACE score in the target and mixed region. Then, as the FAR reaches 1% (and an ACE score equal to 0), the next detection order should move from the high MF score to the low MF score. A flowchart of the proposed method is shown in Figure 5.8.

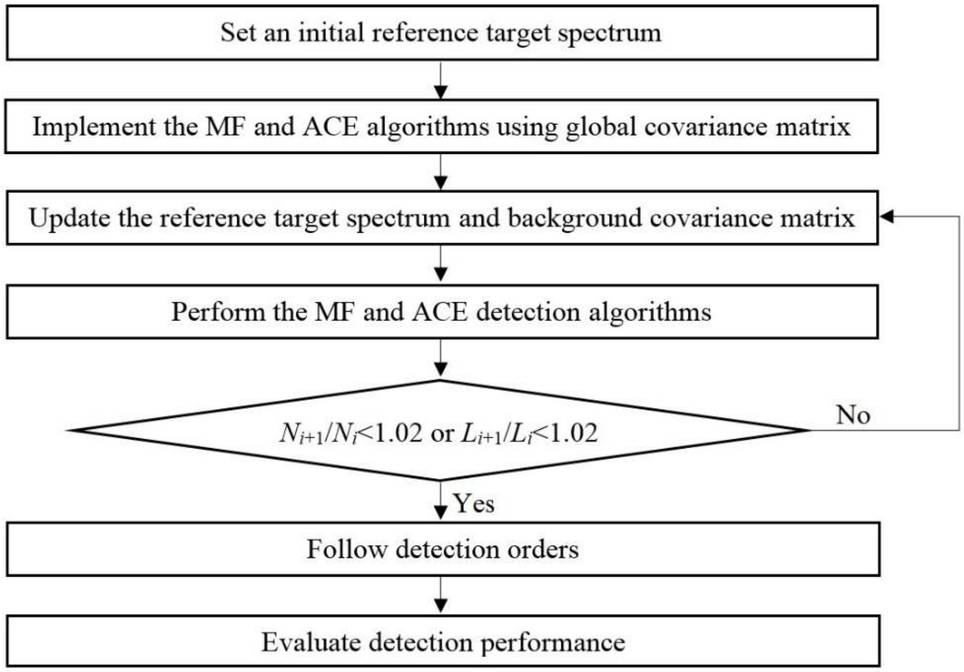

Figure 5.8: Flowchart of the proposed method

Although there is spectral variation of targets, a large amount of bands can compensate for this. Hundreds of bands extend to a high dimensional space. In the high dimensional whitened data space, any specific material should have its own hypercone. This provides a good opportunity to differentiate the target of interest from background and other abnormalities. For one specific target, although the subpixel targets have some variation, they should fall inside its hypercone and follow some distribution principles. The essence of the proposed method is finely adjusting the direction of the hypercone according to the target distribution principles and making the hypercone cover the maximum number of targets.

6. EXPERIMENTS AND RESULTS

The effectiveness of the proposed method for subpixel target detection is demonstrated in this chapter. The experimental model is constructed in Section 6.1. Then, two synthetic and two real hyperspectral datasets are applied in the experiments and the results are compared to those of other counterpart methods.

6.1 Experimental model

The first three HSI datasets used in the experiments are originally taken from the Jet Propulsion Lab (JPL) of the NASA [65] and the spectral bandwidth of each band is approximately 10 nm. The first dataset is "Cuprite," the second dataset is "Low Altitude," and the third dataset is "Moffett Filed." These images were collected by the AVIRIS, which operates in the Visible to Near Infrared and Short-Wave Infrared range of 400 nm to 2500 nm. However, only 172 of 224 spectral bands are selected for the experiments by discarding some water absorption and noisy bands. The selected spectral bands are the 3rd to 43rd, 45th to 60th, 67th to 80th, 86th to 105th, 121st to 151st, 172nd to 173rd and 177th to 224th (Table 6.1). All of these images are then cropped into the regions of interest with a pixel size of 512×512.

Table 6.1: Band selection for the original hyperspectral data

Adopted bands	Number of adopted bands	Excluded bands	Excluded wavelength (nm)
3-43	41	1-2	365-376
45-60	16	44	763
67-80	14	61-66	928-976
86-105	20	81-85	1120-1158
121-151	31	106-120	1343-1483
172-173	2	152-171	1802-1968
177-224	48	174-176	1998-2018

In Experiment A and B, two synthetic datasets are tested to evaluate the newly developed method. A target implantation strategy that has been successfully used for performance evaluation in previous developments is applied to the original datasets [53]. First, signatures for water and vegetation are extracted from AVIRIS data “Moffett Field.” Then, water spectra and vegetation spectra are implanted into “Cuprite” image and “Low Altitude” image using the LMM, respectively.

A traditional detection method (TDM) is introduced to compare the performance, and can be described as follows:

First, PCA transformation is performed to solve for the covariance matrix and eigen values. Each eigen value is normalized by dividing the sum of all. If the sum of the first n normalized eigen values reaches a threshold of 0.999, then the number n is considered as the number of endmembers. Second, N-FINDR is performed to extract the endmembers. The extracted spectra are matched to the reference spectrum, which is the average of high abundance target spectra that is known in the scene, using the SAM. The endmember with the minimum angle compared to the reference spectrum is considered as the target endmember. Third, the RXD algorithm is applied to evaluate the background covariance matrix. The RXD threshold is set to the value that detects the number of abnormalities approximate to the targets present in the scene. Finally, the MF and ACE detection algorithms are performed using the extracted target endmember and the RXD estimated covariance matrix.

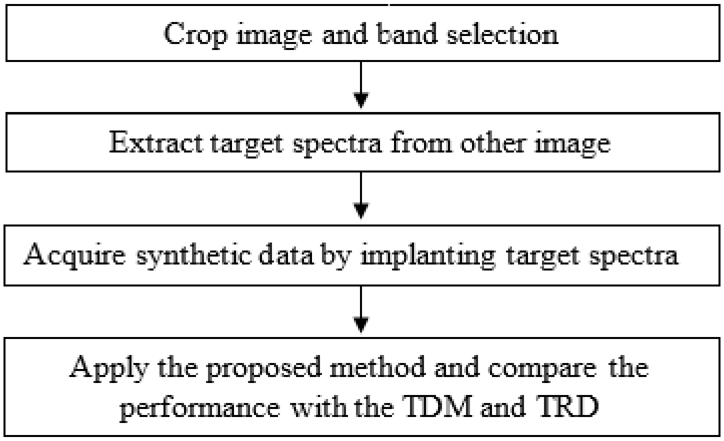

Figure 6.1: Flowchart for synthetic image experiment

For the proposed method in synthetic data, one to five random target spectra from the high abundance target samples are selected. As the insertion points are known, ground-truth image is also known. Then the detection performance under a certain false alarm is easy to calculate. Finally, the results are compared with the counterpart methods (Figure 6.1). As the performance of TDM is much worse than the proposed method, another method, Traditional RXD background estimated Detector (TRD), using the best target spectrum of the proposed method and the RXD covariance matrix, is also applied to evaluate the effectiveness of the MF background evaluation.

Although a synthetic image can provide a totally controllable environment for evaluating the performance of the proposed detector, one of the main concerns is how to model it as closely as possible to the real-world image, reduce the bias, and provide meaningful results. The first dataset introduces a scenario with 8000 low abundance (1%-3%) target pixels and 2000 high abundance (60%-95%) target pixels which are presented as 25 integrated panels. In the second dataset, 5000 of high abundance target pixels and 5000 of low abundance target pixels are inserted into the image with 100 panels. The inserted target spectra are randomly selected from the pool of target samples.

This experimental model could simulate target variations in the real world, and could also model the co-existence of high and low abundance targets.

The detection performance is evaluated using ROC log curves and average DR, which are common metrics for detection evaluation [53]. Detection results under a certain FAR, as well as pixel distribution in hybrid detection space are also provided to show the effectiveness of the proposed method. The high abundance targets are likely to be detected, so in the synthetic experiments, the DR only refers to the low abundance targets. In this way, detection performance of low abundance targets could be evaluated more accurately than using overall DR.

For the real datasets, as the ground-truth images are unknown, the detection results at a certain FAR for proposed method is compared with that of TRD by observation. It would be better to have the high spatial resolution image for these two real HSI datasets to determine if the detected pixels consist of the target of interest. However, it is not easy to find such data. Because a pixel is more likely to be a target if the majority of its surrounding pixels are targets, the detection results of real data experiments could be judged by combining the contexture information of the image. For example, if some soil pixels which are close to the grass are detected as “grass”, these pixels of soil are then considered with some fill factions of grass that are too small to discern by human observation. However, the proposed method can catch the subtle spectral variation in theses pixels and detect them as a target. Although this observation method may produce some error, it is the best way to evaluate the proposed method in detecting the low abundance subpixel targets of real datasets.

6.2 Descriptions of datasets

A. Dataset 1: Inserting water signature into Cuprite image

The spectra data of Cuprite Hills area in southern Nevada were collected in the original image. To generate the synthetic data, 3500 water spectra extracted from Moffett Field are implanted into this scene. The synthetic image is generated using the LMM. A synthetic pixel with a spectral signature Z is the mixture of the desired Target T (T is a randomly picked water spectrum from the extracted samples) with abundance fraction a and background signature B of a selected pixel with abundance fraction $(1-a)$:

$$Z=a\times T+(1-a)\times B \tag{6.1}$$

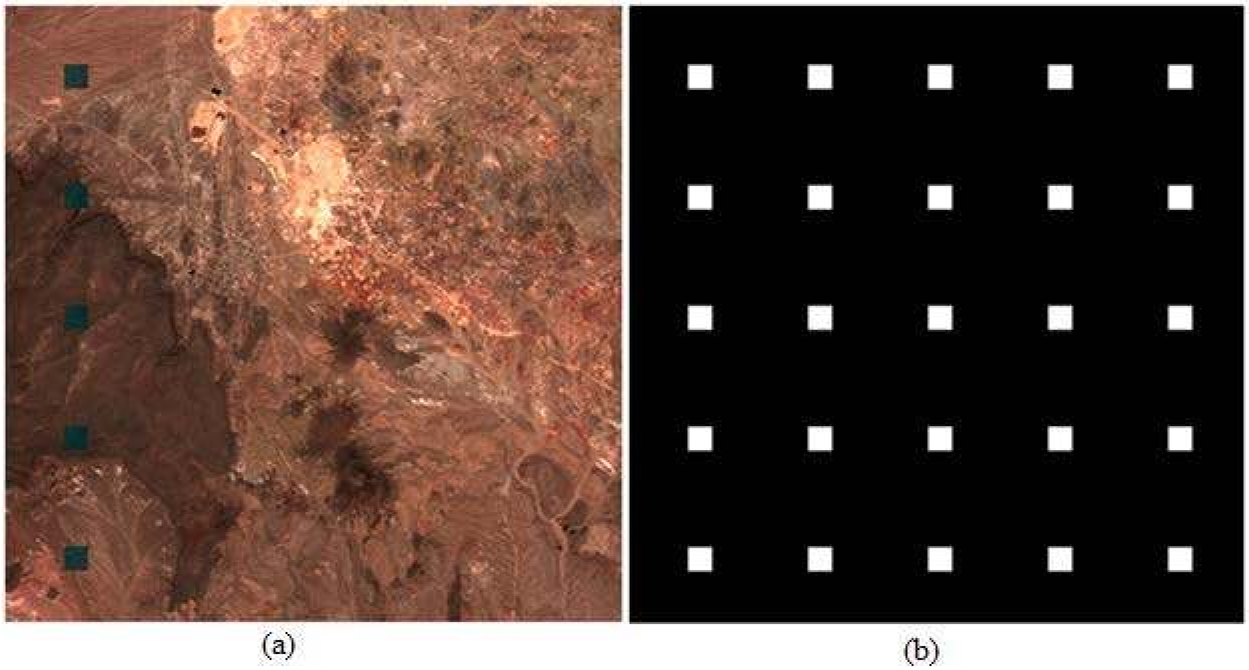

Figure 6.2: Pseudo-color image and the ground-truth map of 25 target panels for Dataset 1

The test image containing targets with different fractions is generated synthetically. In this image, 5×5 target panels are implanted (Figure 6.2 b) in different locations. The abundance fractions of the panels reduce from left to right. The far left column has maximum values randomly generated from the range 0.6-0.95. The abundances for the second, third, fourth and fifth columns are random numbers from 0.025-0.03, 0.02-0.025, 0.015-0.02, and 0.01-0.015, respectively. The main reason for setting abundance 0.6-0.95 for the first column is that it can simulate the existence of high abundance target in the real world. So, this synthetic image consists of 8000 low abundance target pixels and 2000 high abundance target pixels. Figure 6.2 shows the pseudo-color image and the ground-truth map of 25 target panels for Dataset 1. One can see, as the abundances of the right four columns are so small, these targets cannot be discerned in the RGB image.

B. Dataset 2: inserting vegetation signatures into the Low Altitude image

The second hyperspectral image is the commonly-used AVIRIS Low Altitude image. After pre-processing, this image has a spatial dimension of 512×512 pixels with 172 bands. It contains some construction, such as buildings, roads and agricultural fields.

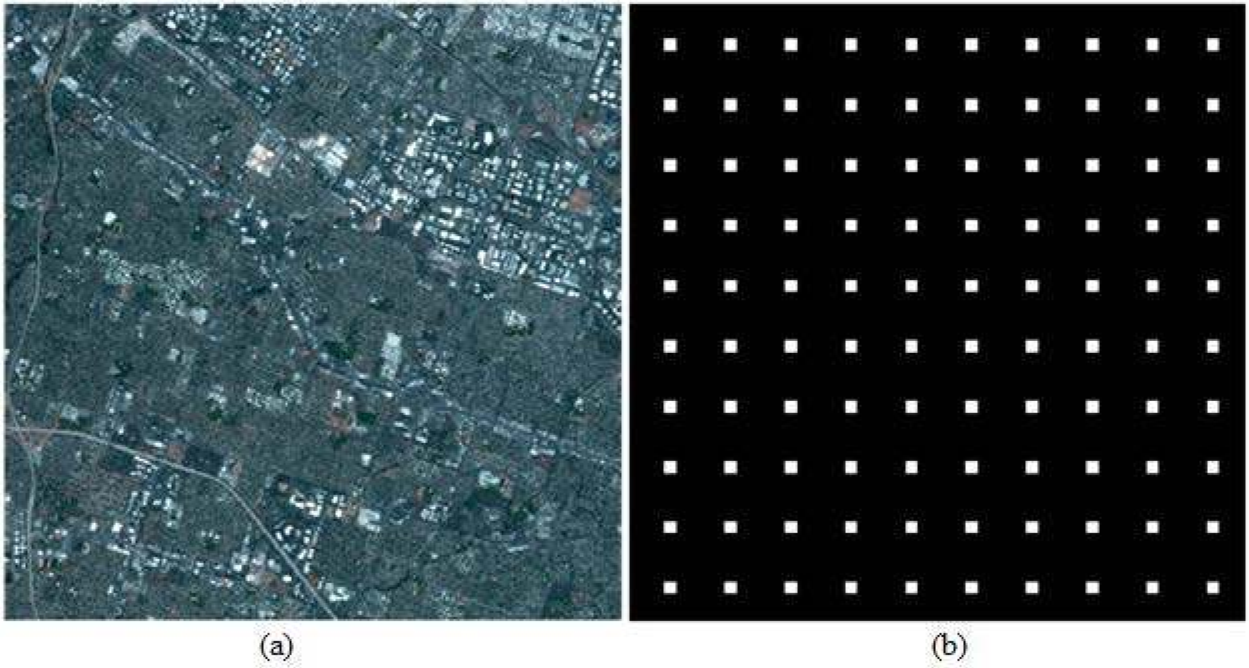
(a) (b)

Figure 6.3: Pseudo-color image and the ground-truth map of targets for Dataset 2

In this image, 10×10 target panels are implanted and each panel consists of 10×10 pixels. The locations of the synthetic pixels are provided in Figure 6.3 b. The synthetic pixels are generated using the LMM model which is used in Dataset 1. New synthetic data are obtained by a linear combination of the original background spectra and the selected target spectra from the target samples (vegetation spectra extracted from Moffett Field). The abundances of the panels increase from left to right: 0.05 0.06 0.07 0.08 0.09 for the left five columns, and 0.55 0.65 0.75 0.85 0.95 for right five columns, respectively. So, this synthetic image consists of 5000 low abundance target pixels and 5000 high abundance target pixels. Figure 6.3 shows pseudo-color image and the ground-truth map for Dataset 2.

C. Dataset 3: Moffett Field

The Moffett Field image shows a very smooth area of water and a fairly homogeneous urban area which is mainly composed of three components: water, soil, and vegetation [66]. Therefore, this dataset is a good example for water and vegetation study.

This Dataset is used to evaluate the performance of the proposed method in detecting subpixel targets of real image. After pre-processing, this image has the spatial dimension of 512×512 pixels, each having 172 bands with the 52 noisiest bands removed.

D. Dataset 4: Pavia University

The fourth dataset used in this experiment is the Pavia University image acquired at the University of Pavia, Italy, using the Reflective Optics System Imaging Spectrometer (ROSIS) sensor [67]. The scene shows an urban area comprised of different buildings, parking lots, roads and other typical human-made constructions, together with trees, green areas, and bare soil. The image size in pixels is 610 × 340, with a spatial resolution of 1.3 m/pixel [68]. The original image has 103 spectral channels covering wavelength range from 0.43 to 0.86 μm. Only 89 channels are preserved for the experiment after discarding 14 noisy spectral bands.

6.3 Experimental results and discussion

A. Dataset 1

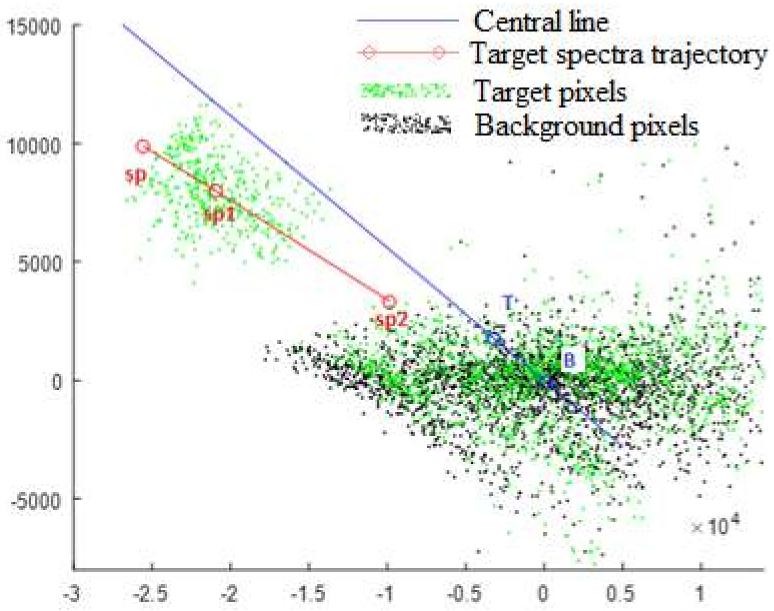

Figure 6.4: Iterative reference target spectrum improvement for Dataset 1

Figure 6.4 shows the iterative reference target spectrum improvement. This image transforms the high dimensional data into a two-dimensional data plot, using PCA. B is the center of the background; T is the center of the target; black dots are background pixels; green dots are target pixels; and *sp, sp1, sp2* and *sp3* are the reference spectra acquired using the proposed method. The trajectory of the reference target spectra gets closer and closer to the central line BT. From Table 6.2, one can see *sp2* is the best target spectrum, according to the iterative terminal conditions provided in Chapter V, and has the minimum angle to the line BT. The detection performance for different reference spectra at different FARs are provided in Table 6.3. *sp2* also has the best average detection rate of all the spectra.

Table 6.2: Evaluation of spectra for Dataset 1

Reference spectrum	sp	sp1	sp2	sp3
Target Detected	2142	7390	8302	8715
Max(MF)	15.6	158	222	226
Angle	2.28	1.19	1.01	/

Table 6.3: Detection rates for Dataset 1

Spectrum	FAR	0.02%	0.05%	0.1%	0.2%	0.5%	1%	2%	5%	Mean
sp	MF	0	0.0006	0.0014	0.0066	0.0236	0.0414	0.0739	0.154	0.0377
	ACE	0	0.0006	0.0015	0.0029	0.0094	0.0174	0.0299	0.0696	0.0164
sp1	MF	0.023	0.1274	0.3511	0.5326	0.6975	0.7875	0.8578	0.9197	0.5371
	ACE	0.3535	0.4387	0.51	0.5751	0.659	0.7205	0.781	0.8524	0.6113
sp2	MF	0.005	0.0709	0.2285	0.4636	0.6774	0.7833	0.8576	0.9231	0.5012
	ACE	0.3602	0.4367	0.5101	0.5814	0.6794	0.7496	0.8067	0.8766	0.6251
sp3	MF	0.0014	0.0236	0.1278	0.3706	0.6362	0.7705	0.8518	0.9223	0.4630
	ACE	0.301	0.374	0.464	0.5439	0.6646	0.7426	0.807	0.8789	0.597
HDS	Fusion	0.3671	0.4456	0.5268	0.6022	0.7175	0.7833	0.8576	0.9231	0.6529

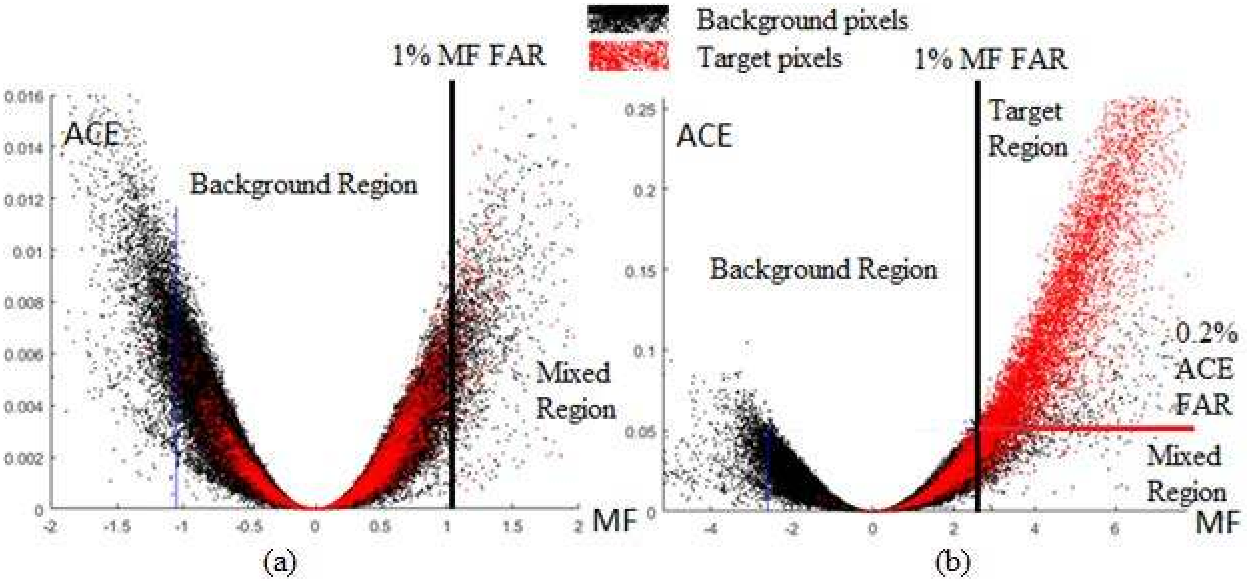

Figure 6.5: Background-Target separability (a) before and (b) after applying the proposed method for Dataset 1

Target-background separability for initial as well as best detection results of the proposed method are shown in the hybrid detection space (Figure 6.5). The black dots stand for background pixels, while red dots stand for target pixels. The background is always constrained in a small region and is symmetrical about the *y* axis during the iterative process. The subpixel targets are mixed with the background at the beginning; however, they achieve better separability after applying the proposed method, because most of them escape from the background region.

Finally, the detection performance of the proposed method, shown in Table 6.4, is compared with the TDM and TRD methods. TDMF and TDMA mean MF and ACE algorithms under TDM conditions, respectively. TRDM and TRDA mean MF and ACE algorithms under TRD conditions, respectively. HDS means the proposed method. ROC log curves comparison is shown in Figure 6.6. The blue line is the HDS; the red line is the TRDM; the magenta line is the TRDA; the black line is the TDMF; and the green line is the TDMA. Both the ROC curve and the average detection rate show that the proposed method has a better performance than the TDM and TRD.

Table 6.4: Detection rates comparison for Dataset 1

FAR	0.02%	0.05%	0.1%	0.2%	0.5%	1%	2%	5%	Mean
TDMF	0.0001	0.0006	0.0018	0.0031	0.011	0.0256	0.057	0.1411	0.0300
TDMA	0	0.0004	0.0016	0.0045	0.0108	0.0209	0.0397	0.089	0.0209
TRDM	0	0.003	0.0343	0.1251	0.3147	0.4427	0.5669	0.7	0.2733
TRDA	0.0454	0.0833	0.1325	0.1854	0.2574	0.3049	0.3596	0.4465	0.2269
HDS	0.3671	0.4456	0.5268	0.6022	0.7175	0.7833	0.8576	0.9231	0.6529

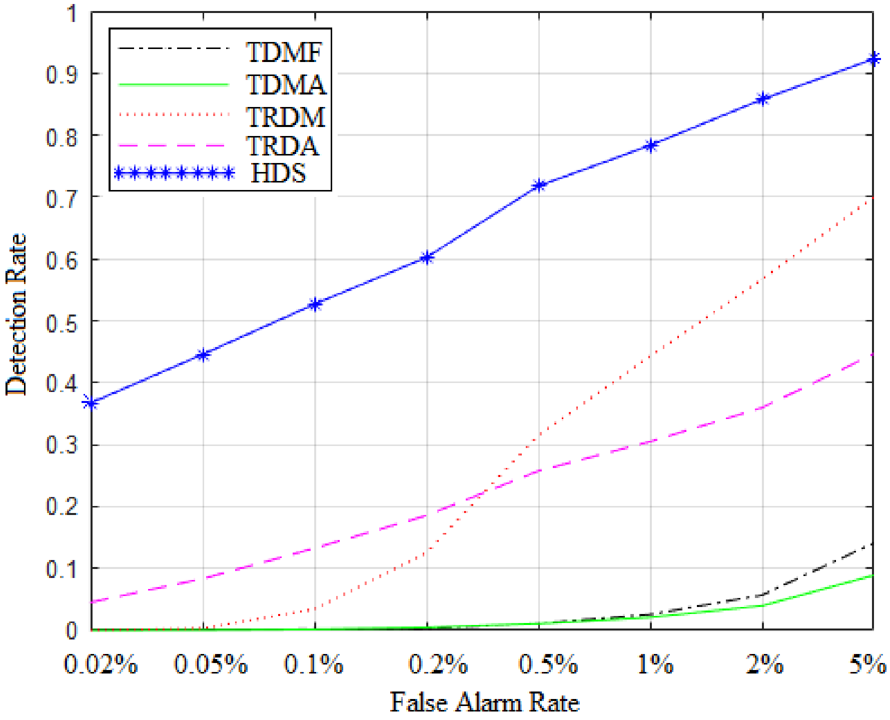

Figure 6.6: ROC curve comparison for Dataset 1

Figure 6.7 shows the detection results for the TRDM and the hybrid algorithm at 1% FAR. For high abundance targets, both algorithms can detect all of the targets. For low abundance targets, the right two columns of the targets in the left image are hardly detected. However, the middle three columns in the right image are almost detectable. This indicates that the detection performance of the proposed method is much better than other counterparts in Dataset 1 at 1% FAR.

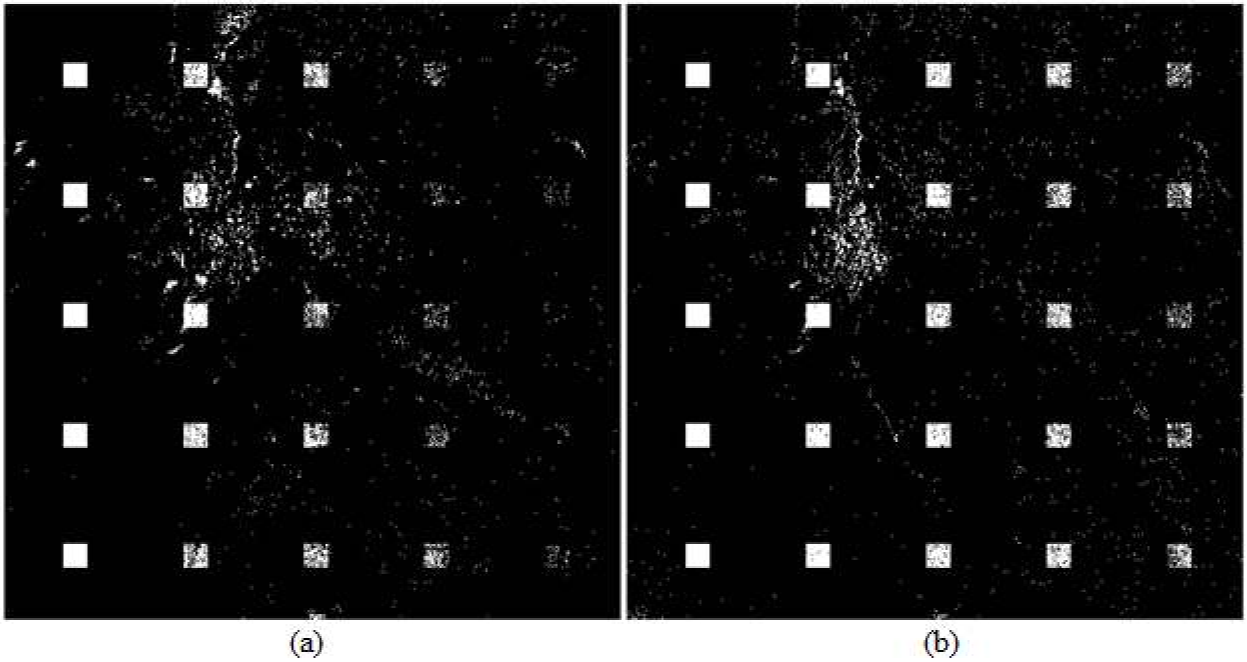

(a)

(b)

Figure 6.7: Detection images comparison for Dataset 1 at 1% FAR
(a) TRDM; (b) Proposed method

B. Dataset 2

The iterative improvement of the reference target spectrum is shown in Figure 6.8. *sp, sp1, sp2, sp3* and *sp4* are the reference spectra acquired using the proposed method. As one can see, the trajectory gets closer and closer to the central line. Table 6.5 shows the evaluation of the spectra. *sp4* is the one that satisfies the terminal conditions. Detection performances under different FARs are shown in Table 6.6. *sp4* yields the best average detection rate among all of the spectra.

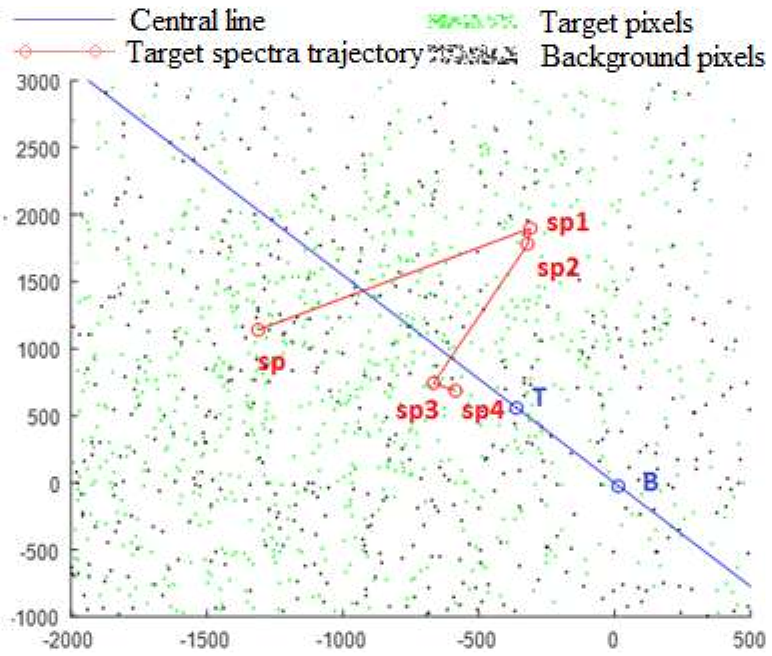

Figure 6.8: Iterative reference target spectrum improvement for Dataset 2

Table 6.5: Evaluation of spectra for Dataset 2

Reference Spectrum	sp	sp1	sp2	sp3	sp4	sp5
Target Detected	1249	4878	7613	9145	9346	9359
Max(MF)	10	43	108	152	173	172
Angle	18.85	14.94	12.61	2.63	1.06	/

Table 6.6: Detection rates for Dataset 2

Spectrum	FAR	0.02%	0.05%	0.1%	0.2%	0.5%	1%	2%	5%	mean
sp	MF	0.0002	0.0002	0.0012	0.0024	0.0078	0.0182	0.036	0.0874	0.0192
	ACE	0.0006	0.0014	0.002	0.0044	0.0096	0.0172	0.0306	0.065	0.0164
sp1	MF	0.0152	0.0872	0.1726	0.2512	0.3338	0.3886	0.4516	0.5406	0.2801
	ACE	0.181	0.2104	0.231	0.2668	0.3174	0.359	0.4078	0.4882	0.3077
sp2	MF	0.202	0.4056	0.5236	0.5998	0.6702	0.7096	0.7512	0.8072	0.5837

	ACE	0.4988	0.5344	0.5726	0.6036	0.6502	0.682	0.7172	0.7722	0.6289
sp3	MF	0.2938	0.552	0.675	0.756	0.8152	0.8514	0.8764	0.91	0.7162
	ACE	0.678	0.715	0.742	0.768	0.808	0.8334	0.8554	0.886	0.7857
sp4	MF	0.3164	0.5746	0.7102	0.7968	0.8558	0.8846	0.9124	0.936	0.7484
	ACE	0.7348	0.7682	0.79	0.8142	0.849	0.8734	0.8962	0.9222	0.831
HDS	Fusion	0.745	0.7798	0.8006	0.831	0.8642	0.8846	0.9124	0.936	0.8442

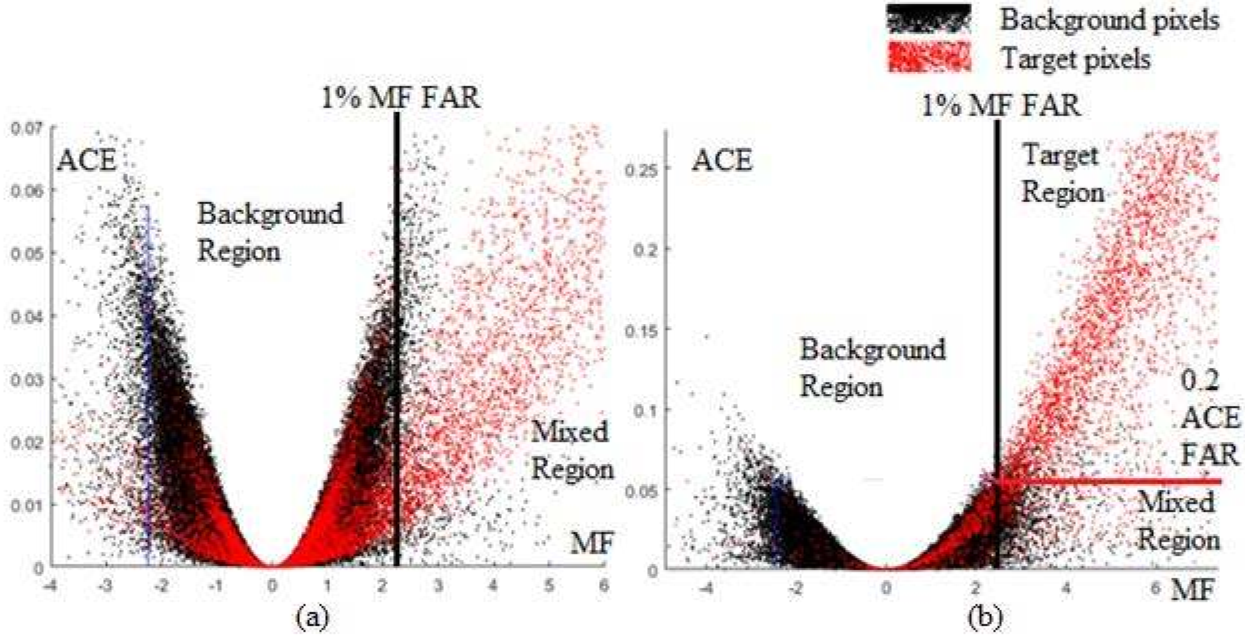

Figure 6.9: Background – Target separability (a) before and (b) after apply the proposed method for Dataset 2

Figure 6.9 shows the target-background separability for initial and best detection results of proposed method in the hybrid detection space. The background is always constrained in the background region and is symmetrical about the *y* axis during the iterative process. The results indicate that better separability can be achieved by applying the proposed method. Most of the subpixel targets have high contrast in respect to those of the background in the final results.

Table 6.7: Detection rates comparison for Dataset 2

FAR	0.02%	0.05%	0.1%	0.2%	0.5%	1%	2%	5%	Mean
TDMF	0.001	0.0014	0.0014	0.0036	0.0072	0.0106	0.0232	0.0502	0.0123
TDMA	0	0.001	0.002	0.0038	0.0054	0.012	0.0206	0.047	0.0115
TRDM	0.1814	0.3866	0.5372	0.6562	0.7898	0.851	0.8948	0.9298	0.6534
TRDA	0.6496	0.6896	0.7152	0.7418	0.7816	0.811	0.8414	0.8768	0.7634
HDS	0.745	0.7798	0.8006	0.831	0.8642	0.8846	0.9124	0.936	0.8442

Table 6.7 shows the comparison of detection performances of the proposed, TDM and TRD methods. For illustrative purposes, Figure 6.10 shows the ROC log curves corresponding to the detection results reported in Table 6.7. Generally, the proposed method can achieve better performance compared to the TDM and TRD methods.

Figure 6.11 shows the detection results for the TRDA and hybrid algorithm at 0.1% FAR. For high abundance targets, both algorithms can detect most of targets. For low abundance targets, more pixels inside the square panels are detected in Figure 6.11b than Figure 6.11a. This indicates the detection performance of the proposed method is better than its counterparts for Dataset 2 at 0.1% FAR.

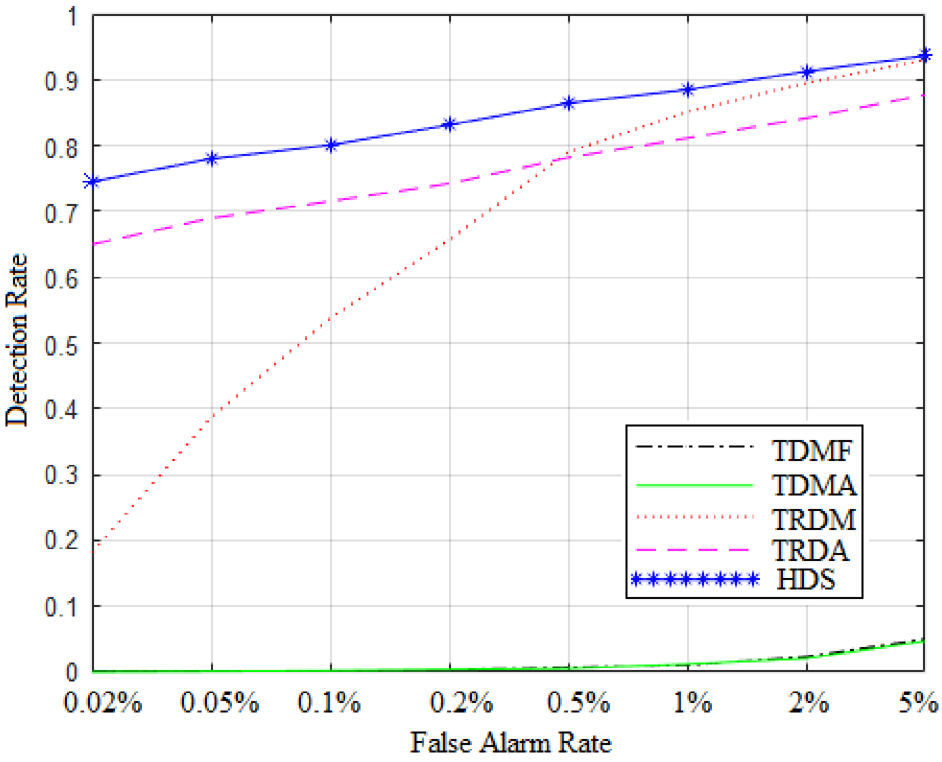

Figure 6.10: ROC curve comparison for Dataset 2

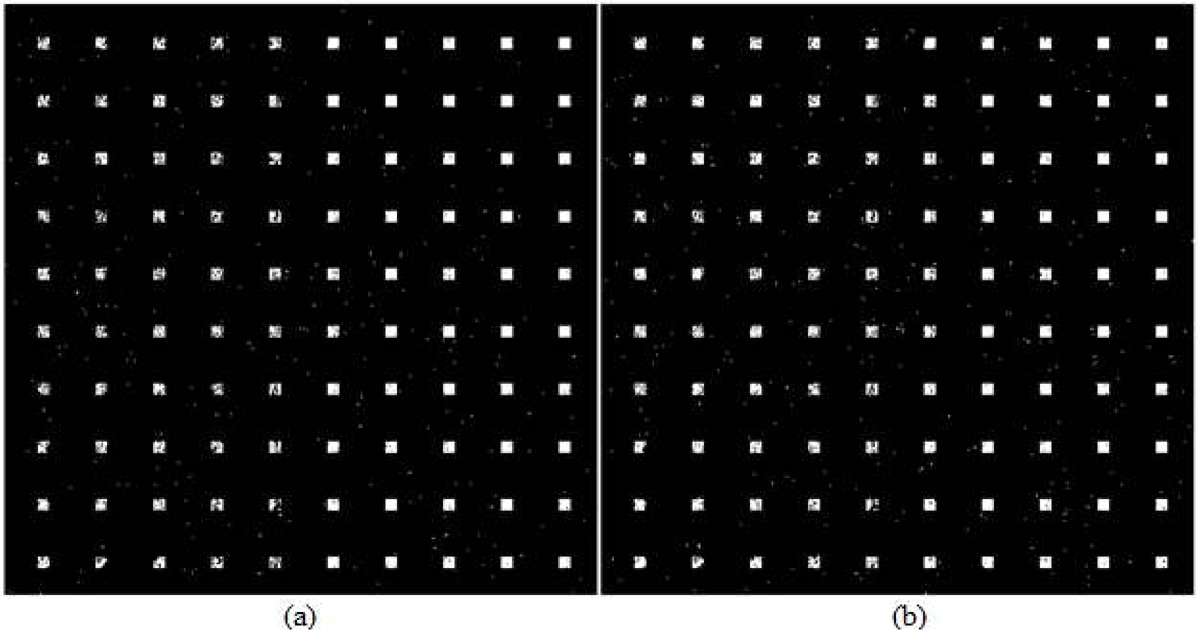

Figure 6.11: Detection results comparison for Dataset 2 at 0.1% FAR

(a) TRDA; (b) Proposed method

C. Dataset 3

In this section, the Moffett Filed data collected by the AVIRIS are used for experiment evaluation of the proposed detector in real scenarios. Vegetation in the scene is considered as the target of interest.

Figure 6.12 shows the iterative improvement of the reference target spectrum. Because the background and target truth maps are unknown, the final target region is assumed to include all the targets; the final background region is assumed to include all the background. At this point, the centers T and B can be calculated. Generally, the trajectory of the reference target spectra gets closer and closer to the central line. Table 6.8 evaluates the spectra acquired from the proposed method. *sp8* is the one that satisfies the terminal conditions.

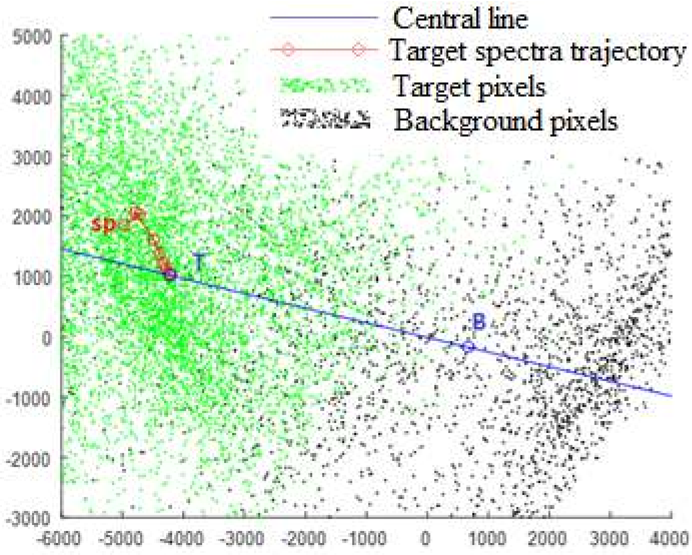

Figure 6.12: Iterative reference target spectrum improvement for Dataset 3

Table 6.8: Evaluation of spectra for Dataset 3

Reference Spectrum	sp	sp1	sp2	sp3	sp4	sp5	sp6	sp7	sp8	sp9
Target Detected	1722	8971	15980	23171	28583	32021	34823	36352	37499	37261
Max(MF)	5.1	9.3	13.8	17	19.7	21.3	22.9	23.9	24.6	24.3
Angle	46.21	21.49	15.28	8.78	5.15	2.95	1.67	0.663	0	/

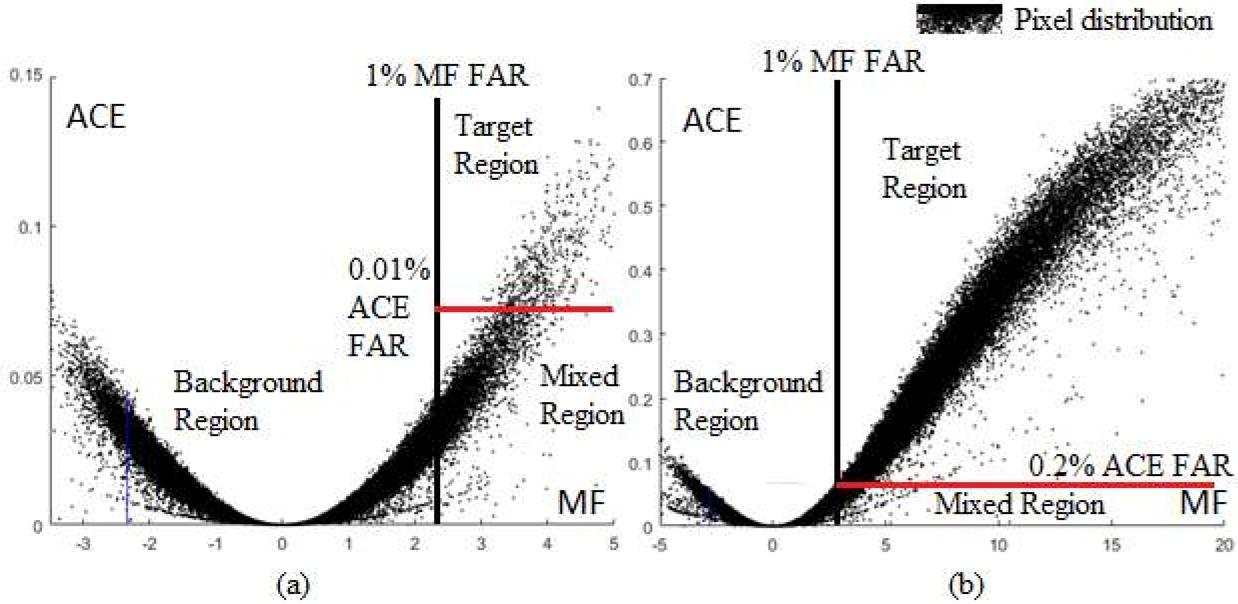

Figure 6.13: Background-Target separability (a) before and (b) after applying the proposed method for Dataset 3

Pixel distribution in the hybrid detection space for initial and final detection results of the proposed method are shown in Figure 6.13. In the Figure 6.13b, potential targets escape from the background region. Figure 6.14 compares the detection results of the TRDM and proposed method at 0.1% FAR. The regions circled in red contain the low abundance targets (mixture of vegetation and soil). The proposed method can detect more of the low abundance targets than the TRDM. Obviously, the proposed method overrides the TRDM.

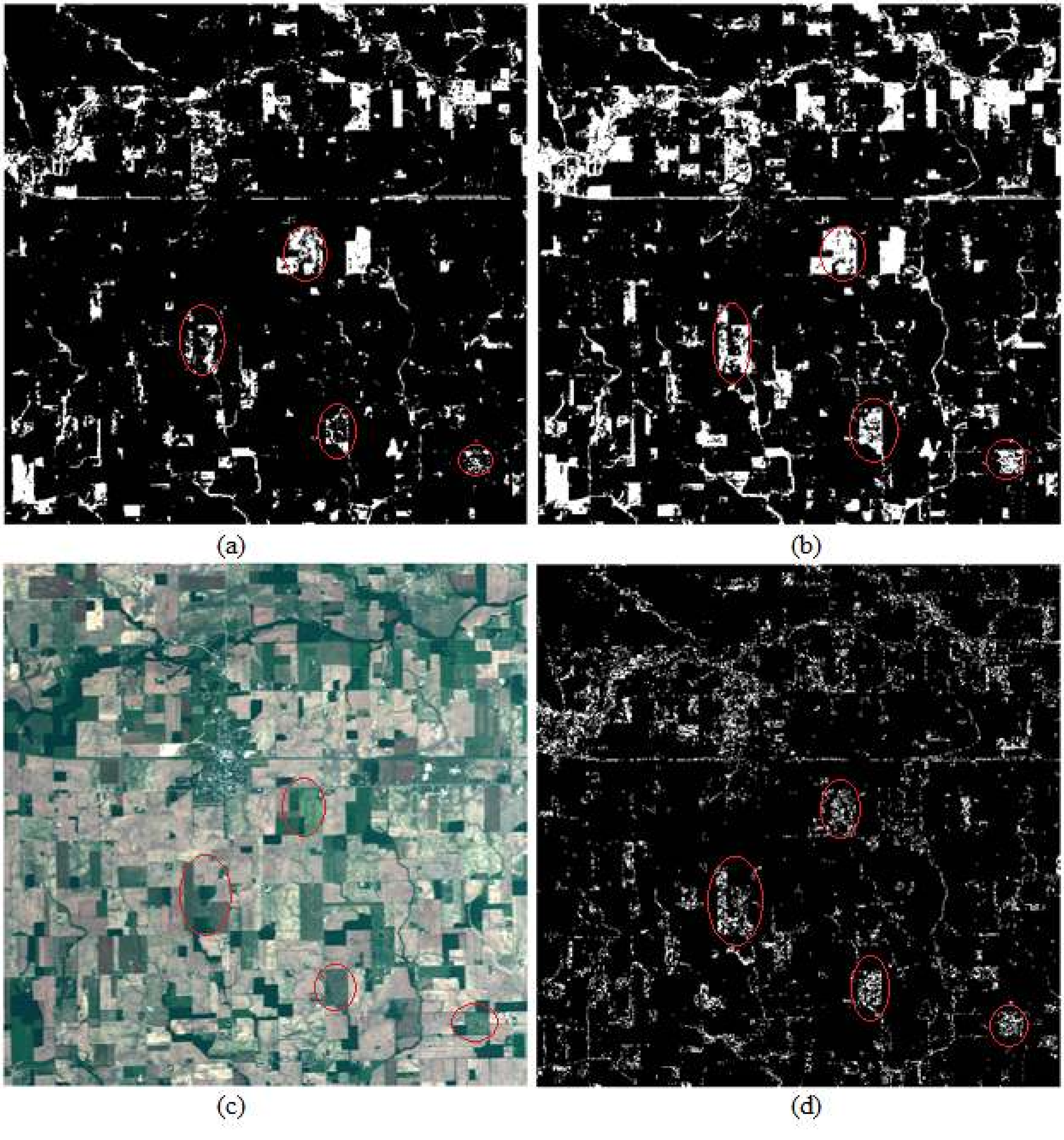

Figure 6.14: Detection results comparison for Dataset 3

(a) TRDM with 0.1% FAR; (b) Proposed method with 0.1% FAR; (c) Pseudo-color image of Dataset 3; (d) Image of the difference between (b) and (a)

D. Dataset 4

In this section, the Pavia University image is used for experiment evaluation of the proposed detectors in real scenarios. The Meadow is considered as the target.

Table 6.9 shows the evaluation of the spectra acquired from the proposed method. *sp13* is the best spectrum according to the terminal conditions. Initial and final background-target separability in the hybrid detection space is shown in Figure 6.15. The potential targets escape from the background region in Figure 6.15b. As the ground truth image is unknown, the pixels in the final target region are considered to contain all the targets and the pixels in background region are considered to contain all the background. Then, the centers T and B can be determined and the errors can be minimized. From Figure 6.16, the reference target spectra get closer and closer to the central line as the iterative process proceeds.

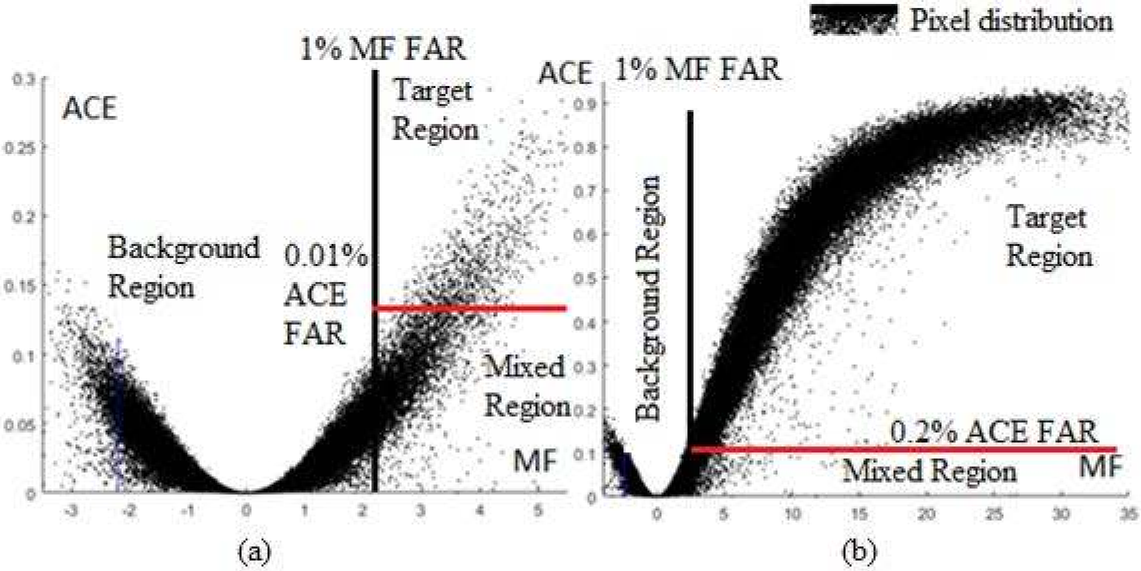

Figure 6.15: Background-Target separability (a) before and (b) after applying the proposed method for Dataset 4

Table 6.9: Evaluation of spectra for Dataset 4

Reference Spectrum	sp	sp1	sp2	sp3	sp4	sp5	sp6	sp7	sp8	sp9	sp10	sp11	sp12	sp13	sp14
Target Detected	1538	4198	6265	8488	9449	10304	10976	12193	13642	15035	16144	17158	17708	18433	18737
Max(MF)	5.7	7.2	7.9	8.5	8.7	8.9	9	9.2	9.5	9.7	9.9	10.6	11	11.3	11.5
Angle	72.05	58.99	51.18	44.58	40.72	37.71	34.26	30.30	25.17	18.30	11.18	6.02	2.52	0	/

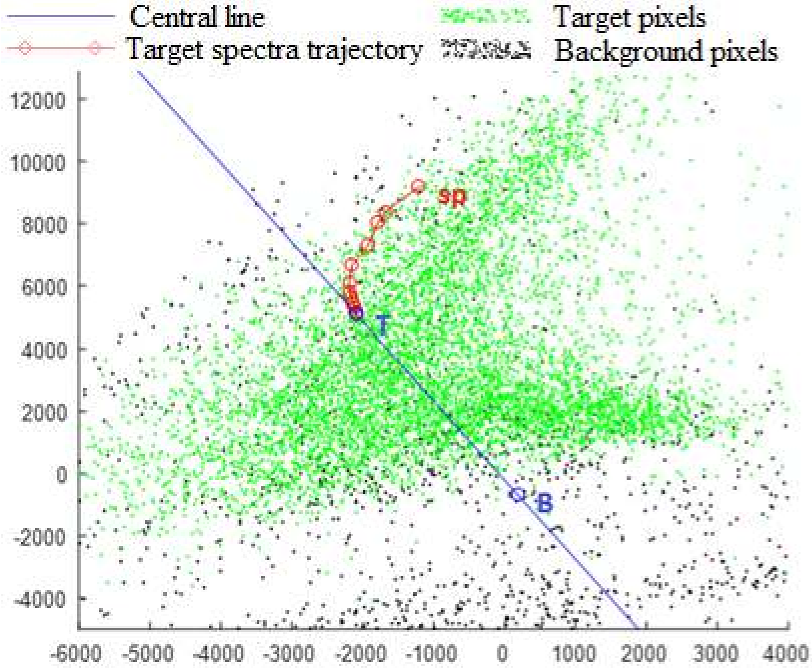

Figure 6.16: Iterative reference target spectrum improvement for Dataset4

Figure 6.17 shows the detection results for performance comparison of the TRDM and proposed method at 1% FAR. The proposed method overrides the TRDM in detecting the low abundance targets (circled in red) obviously.

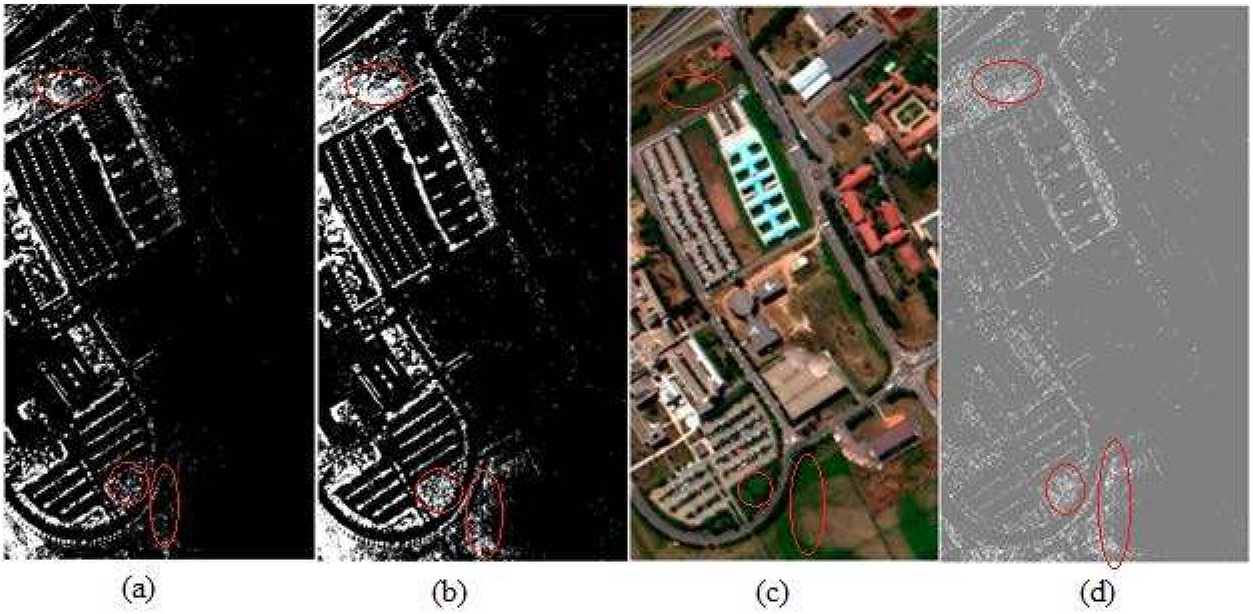

Figure 6.17: Detection results comparison for Dataset 4
(a)TRDM with 1% FAR; (b) Proposed method with 1% FAR; (c) Pseudo-color image of Dataset 4; (d) Image of the difference between b and a

While applying the proposed method, both the number of detected targets inside the hypercone, and the average of top MF scores increase. However, as the updated spectrum gets closer to the central line, the increase rates slow down and the angle between the new spectrum and the central line decrease. When the evaluation metrics reach terminal conditions, the best target spectrum usually leads to the best detection performance. Furthermore, the MF background evaluation excludes most of the targets from the background region and yields to better statistics. During the iterative process, the background is always constrained in the background region; subpixel targets escape from the background region and lead to better separability. Therefore, the proposed method has the best performance among all algorithms used in the experiment.

The traditional detection method used the N-FINDR target extraction and RXD background evaluation has the worst performance due to errors in extracted target spectrum and the background statistics. The detection results of the traditional method can vary and depend greatly on the quality of the extracted target spectrum. The actual target spectrum may not be extracted due to a lack of full pixel targets in the scene. Moreover, a single pixel spectrum from the image could not reflect the spectral variation of the targets, so that the traditional method does not have very good performance. Although the endmember extraction technique can be improved using such techniques as NMF, the computational cost would also increase.

The TRD having better performance than the TDM implies the importance of the reference target spectrum. The fact that the proposed method performs better than the TRD indicates that MF background evaluation is superior to RXD background evaluation.

The detection algorithm developed in this work provides a great improvement with regard to its traditional counterparts. In general, these four experiments demonstrate the ability of the hybrid algorithm to achieve the best detection performance by gradually improving the reference target spectrum, which can represent target spectral variability, and improving target-free background modeling.

The calculation time for six iterations of the proposed method is 377 seconds, while the calculation time for the traditional method using N-FINDR endmember extraction is 395 seconds, both running in MATLAB^{TM} R2016a with i7-4790s CPU and 8GB RAM. In general, the proposed method does not increase the computational cost.

7. CONCLUSIONS AND FUTURE WORK

The MF and ACE have been widely applied in HSI target detection since the 1990s. However, how to characterize the background and target is always an important issue while employing these algorithms. A hybrid detection space constructed by these two simple algorithms is developed to extract a better target and background representation. The principle of the hybrid detection space is transforming original data to high dimensional whitened data first, and then transforming the high dimensional data to the visualized hybrid detection space. Since background distribution in hybrid detection space is constrained to a small area, targets are easy to separate from the background.

The proposed MF background evaluation aims at a better representation of background. As most of the targets are excluded from the background samples, the proposed method can lead to a more accurate covariance matrix and better suppress the background. Furthermore, detection region calculated with an improved target spectrum can cover a maximum number of targets at a given false alarm rate, thus improve the separability of the detection algorithm.

The experimental results, conducted using both synthetic and real hyperspectral datasets, indicate that the proposed method provides better performance than the traditional counterparts, particularly for the detection of sub-pixel targets.

The conventional methods, like statistical methods, representation methods, and subspace methods, highly rely on the background and target sample size. However, the sample size may be limited in most applications. The proposed method is different from the conventional ones in many aspects. It does not require calibration or HU before applying the detection algorithm and does not rely on the standard library. These simplify the detection process and reduce the errors in pre-processing. For the initial detection, the reference target spectrum can be any high abundance target randomly picked from the scene, and the background covariance matrix can be evaluated by the whole image. Therefore, the proposed method is generally applicable. Experiments also show promising results in low abundance (as low as 1%-10%) target detection. This proves the high spectral resolution properties of the HSI indeed compensate for the low spatial resolution. Target detection by HSI can cover a much greater area, meanwhile improving the detection performance. Furthermore, as the MF and ACE are simple algorithms, this makes it possible for real time processing. The hybrid algorithm can be applied in detecting water resources, vegetation and oil contamination in a large scene. All these benefits would help in the development of hyperspectral detection applications.

Some issues still need further study to improve the proposed method: because the iterative process is time consuming, reducing the computational cost of the iterative process and making it converge faster become important. Moreover, improving the MVN model of the background by kernelizing the data and combining the detection results with contexture information are good directions to further improve the performance.

Another shortcoming of the proposed method is that it is only applicable in case of many (above thousands) targets existing in the scene because the iterative improvement is based on the target distribution assumption inside the hypercone. If the target sample size is limited, then the target distribution assumption would not hold. Nonetheless, in most remote sensing cases, which are looking for targets like mineral resources, water, or pollution, the proposed method still has a significant improvement compared to the traditional methods.

REFERENCES

[1] Manolakis, D., Marden, D., & Shaw, G. A. (2003). Hyperspectral image processing for automatic target detection applications. Lincoln laboratory journal, 14(1), 79-116.

[2] Gu, Y., Wang, C., Wang, S., & Zhang, Y. (2011). Kernel-based regularized-angle spectral matching for target detection in hyperspectral imagery. Pattern Recognition Letters, 32(2), 114-119.

[3] Adams, J. B., Smith, M. O., & Johnson, P. E. (1986). Spectral mixture modeling: A new analysis of rock and soil types at the Viking Lander 1 site. Journal of Geophysical Research: Solid Earth, 91(B8), 8098-8112.

[4] Craig, M. D. (1990, October). Unsupervised unmixing of remotely sensed images. In *Proceedings of the Fifth Australasian Remote Sensing Conference* (pp. 324-330).

[5] Winter, M. E. (1999, October). N-FINDR: An algorithm for fast autonomous spectral end-member determination in hyperspectral data. In *SPIE's International Symposium on Optical Science, Engineering, and Instrumentation* (pp. 266-275). International Society for Optics and Photonics.

[6] Nasrabadi, N. M. (2008, April). Regularization for spectral matched filter and RX anomaly detector. In *SPIE Defense and Security Symposium* (pp. 696604-696604). International Society for Optics and Photonics.

[7] Reed, I. S., & Yu, X. (1990). Adaptive multiple-band CFAR detection of an optical pattern with unknown spectral distribution. *IEEE Transactions on Acoustics, Speech, and Signal Processing*, *38*(10), 1760-1770.

[8] Mehmood, A., & Nasrabadi, N. M. (2010, April). Anomaly detection in wavelet domain for long-wave FLIR imagery. In *SPIE Defense, Security, and Sensing* (pp. 76960S-76960S). International Society for Optics and Photonics.

[9] Kwon, H., & Nasrabadi, N. M. (2005). Kernel RX-algorithm: A nonlinear anomaly detector for hyperspectral imagery. *IEEE Transactions on Geoscience and Remote Sensing*, *43*(2), 388-397.

[10] Kwon, H., & Nasrabadi, N. M. (2006). Kernel matched subspace detectors for hyperspectral target detection. *IEEE transactions on pattern analysis and machine intelligence*, *28*(2), 178-194.

[11] Kruse, F. A., Lefkoff, A. B., Boardman, J. W., Heidebrecht, K. B., Shapiro, A. T., Barloon, P. J., & Goetz, A. F. H. (1993). The spectral image processing system (SIPS)—interactive visualization and analysis of imaging spectrometer data. *Remote sensing of environment*, *44*(2-3), 145-163.

[12] Li, W., Du, Q., & Zhang, B. (2015). Combined sparse and collaborative representation for hyperspectral target detection. *Pattern Recognition*, *48*(12), 3904-3916.

[13] Robey, F. C., Fuhrmann, D. R., Kelly, E. J., & Nitzberg, R. (1992). A CFAR adaptive matched filter detector. *IEEE Transactions on aerospace and electronic systems*, *28*(1), 208-216.

[14] Conte, E., Lops, M., & Ricci, G. (1995). Asymptotically optimum radar detection in compound-Gaussian clutter. *IEEE Transactions on Aerospace and Electronic Systems*, *31*(2), 617-625.

[15] Scharf, L. L., & Friedlander, B. (1994). Matched subspace detectors. *IEEE Transactions on Signal Processing*, *42*(8), 2146-2157.

[16] Kraut, S., Scharf, L. L., & McWhorter, L. T. (2001). Adaptive subspace detectors. *IEEE Transactions on signal processing*, *49*(1), 1-16.

[17] Broadwater, J. B. (2007). *Physics-based detection of subpixel targets in hyperspectral imagery* (Doctoral dissertation, University of Maryland, College Park).

[18] Harsanyi, J. C., & Chang, C. I. (1994). Hyperspectral image classification and dimensionality reduction: An orthogonal subspace projection approach. *IEEE Transactions on geoscience and remote sensing*, *32*(4), 779-785.

[19] Broadwater, J., Meth, R., & Chellappa, R. (2004, September). A hybrid algorithm for subpixel detection in hyperspectral imagery. In *Geoscience and Remote Sensing Symposium, 2004. IGARSS'04. Proceedings. 2004 IEEE International* (Vol. 3, pp. 1601-1604). IEEE.

[20] Chen, Y., Nasrabadi, N. M., & Tran, T. D. (2011). Hyperspectral image classification using dictionary-based sparse representation. *IEEE Transactions on Geoscience and Remote Sensing*, *49*(10), 3973-3985.

[21] Li, W., & Du, Q. (2015). Collaborative representation for hyperspectral anomaly detection. *IEEE Transactions on Geoscience and Remote Sensing*, *53*(3), 1463-1474.

[22] Li, W., Du, Q., & Xiong, M. (2015). Kernel collaborative representation with Tikhonov regularization for hyperspectral image classification. IEEE Geoscience and Remote Sensing Letters, 12(1), 48-52.

[23] Chen, Y., Nasrabadi, N. M., & Tran, T. D. (2011). Simultaneous joint sparsity model for target detection in hyperspectral imagery. IEEE Geoscience and Remote Sensing Letters, 8(4), 676-680.

[24] Chen, Y., Nasrabadi, N. M., & Tran, T. D. (2013). Hyperspectral image classification via kernel sparse representation. IEEE Transactions on Geoscience and Remote sensing, 51(1), 217-231.

[25] Zhao, C., Li, W., Sanchez-Azofeifa, G. A., Qi, B., & Cui, B. (2016). Improved collaborative representation model with multitask learning using spatial support for target detection in hyperspectral imagery. Journal of Applied Remote Sensing, 10(1), 016009-016009.

[26] Xiong, M., Ran, Q., Li, W., Zou, J., & Du, Q. (2015). Hyperspectral image classification using weighted joint collaborative representation. IEEE Geoscience and Remote Sensing Letters, 12(6), 1209-1213.

[27] Chen, Y., Tran, T. D., & Nasrabdi, N. M. (2012). 19 Sparse Representation for Target Detection and Classification in Hyperspectral Imagery. Signal and Image Processing for Remote Sensing, 375.

[28] Choi, Y., Sharifahmadian, E., & Latifi, S. (2013). Performance analysis of contourlet-based hyperspectral image fusion methods. International Journal on Information Theory, 2(1), 1-14.

[29] Nasrabadi, N. M. (2014). Hyperspectral target detection: An overview of current and future challenges. IEEE Signal Processing Magazine, 31(1), 34-44.

[30] Niu, Y., & Wang, B. (2016). Hyperspectral Anomaly Detection Based on Low-Rank Representation and Learned Dictionary. Remote Sensing, 8(4), 289.

[31] Matteoli, S., Diani, M., & Theiler, J. (2014). An overview of background modeling for detection of targets and anomalies in hyperspectral remotely sensed imagery. IEEE Journal of Selected Topics in Applied Earth Observations and Remote Sensing, 7(6), 2317-2336.

[32] Landgrebe, D. (1997). On information extraction principles for hyperspectral data. Purdue University, West Lafayette, IN, USA, 34.

[33] Broadwater, J., & Chellappa, R. (2007). Hybrid detectors for subpixel targets. IEEE transactions on pattern analysis and machine intelligence, 29(11).

[34] Bioucas-Dias, J. M., Plaza, A., Dobigeon, N., Parente, M., Du, Q., Gader, P., & Chanussot, J. (2012). Hyperspectral unmixing overview: Geometrical, statistical, and sparse regression-based approaches. IEEE Journal of Selected Topics in Applied Earth Observations and Remote Sensing, 5(2), 354-379.

[35] Broadwater, J., Chellappa, R., Banerjee, A., & Burlina, P. (2007, July). Kernel fully constrained least squares abundance estimates. In Geoscience and Remote Sensing Symposium, 2007. IGARSS 2007. IEEE International (pp. 4041-4044). IEEE.

[36] Chang, C. I. (2003). Hyperspectral imaging: techniques for spectral detection and classification (Vol. 1). Springer Science & Business Media.

[37] Manolakis, D., Pieper, M., Truslow, E., Cooley, T., Brueggeman, M., & Lipson, S. (2013, May). The remarkable success of adaptive cosine estimator in hyperspectral target detection. In SPIE Defense, Security, and Sensing (pp. 874302-874302). International Society for Optics and Photonics.

[38] Manolakis, D., Truslow, E., Pieper, M., Cooley, T., & Brueggeman, M. (2014). Detection algorithms in hyperspectral imaging systems: An overview of practical algorithms. IEEE Signal Processing Magazine, 31(1), 24-33.

[39] Multivariate normal distribution. In Wikipedia. Retrieved April 24, 2017, from https://en.wikipedia.org/wiki/Multivariate_normal_distribution

[40] Horvath, S. (2011). Weighted network analysis: applications in genomics and systems biology. Springer Science & Business Media.

[41] Kwon, H., & Nasrabadi, N. M. (2005, June). A comparative study of kernel spectral matched signal detectors for hyperspectral target detection. In Defense and Security (pp. 827-838). International Society for Optics and Photonics.

[42] Chang, C. I., Zhao, X. L., Althouse, M. L., & Pan, J. J. (1998). Least squares subspace projection approach to mixed pixel classification for hyperspectral images. IEEE Transactions on Geoscience and Remote Sensing, 36(3), 898-912.

[43] Marwaha, R., Kumar, A., & Kumar, A. S. (2015). Object-oriented and pixel-based classification approach for land cover using airborne long-wave infrared hyperspectral data. *Journal of Applied Remote Sensing*, *9*(1), 095040-095040.

[44] Liu, D. L., He, G. J., & Zhang, J. Q. (2011, June). Anomaly detection using background prediction in hyperspectral images. In International Symposium on Photoelectronic Detection and Imaging 2011 (pp. 819306-819306). International Society for Optics and Photonics.

[45] Kwon, H., & Nasrabadi, N. M. (2006). Hyperspectral Target Detection Based on Kernels. In Optical Imaging Sensors and Systems for Homeland Security Applications (pp. 287-322). Springer New York.

[46] Cisz, A. (2006). Performance comparison of hyperspectral target detection algorithms.

[47] Davidson, C. E., & Ben-David, A. (2011, October). On the use of covariance and correlation matrices in hyperspectral detection. In Applied Imagery Pattern Recognition Workshop (AIPR), 2011 IEEE (pp. 1-6). IEEE.

[48] Olsen, R. C., Bergman, S., & Resmini, R. G. (1997, October). Target detection in a forest environment using spectral imagery. In Optical Science, Engineering and Instrumentation'97 (pp. 46-56). International Society for Optics and Photonics.

[49] Latifi, S., & Wilson, S. (2016). Maximum Distance Band Selection of Hyperspectral Images. International Journal of Computer Applications, 133(17), 36-43.

[50] Principal component analysis. In Wikipedia. Retrieved April 24, 2017, from https://en.wikipedia.org/wiki/Principal_component_analysis

[51] Das, S., Kundu, J. N., & Routray, A. (2015, December). Estimation of number of endmembers in a Hyperspectral image using Eigen thresholding. In India Conference (INDICON), 2015 Annual IEEE (pp. 1-5). IEEE.
[52] Plaza, A., Martín, G., Plaza, J., Zortea, M., & Sánchez, S. (2011). Recent developments in endmember extraction and spectral unmixing. In Optical Remote Sensing (pp. 235-267). Springer Berlin Heidelberg.
[53] Guo, Q., Zhang, B., Ran, Q., Gao, L., Li, J., & Plaza, A. (2014). Weighted-RXD and linear filter-based RXD: Improving background statistics estimation for anomaly detection in hyperspectral imagery. IEEE Journal of Selected Topics in Applied Earth Observations and Remote Sensing, 7(6), 2351-2366.
[54] Li, Z., Li, J., Zhou, S., & Pirasteh, S. (2015). Comparison of spectral and spatial windows for local anomaly detection in hyperspectral imagery. International Journal of Remote Sensing, 36(6), 1570-1583.
[55] Camacho Velasco, A., Vargas García, C. A., & Arguello Fuentes, H. (2016). A comparative study of target detection algorithms in hyperspectral imagery applied to agricultural crops in Colombia. *Tecnura*, *20*(49), 86-99.
[56] Gao, L., Yang, B., Du, Q., & Zhang, B. (2015). Adjusted spectral matched filter for target detection in hyperspectral imagery. Remote Sensing, 7(6), 6611-6634.
[57] Harsanyi, J. C. (1993). Detection and classification of subpixel spectral signatures in hyperspectral image sequences (Doctoral dissertation, University of Maryland Baltimore County).
[58] Yang, S., & Shi, Z. (2014). SparseCEM and SparseACE for hyperspectral image target detection. IEEE Geoscience and Remote Sensing Letters, 11(12), 2135-2139.
[59] Bioucas-Dias, J. M., Plaza, A., Camps-Valls, G., Scheunders, P., Nasrabadi, N., & Chanussot, J. (2013). Hyperspectral remote sensing data analysis and future challenges. IEEE Geoscience and remote sensing magazine, 1(2), 6-36.
[60] Geng, X., Ji, L., Yang, W., Wang, F., & Zhao, Y. (2016). MF is always superior to CEM. arXiv preprint arXiv:1612.00549.
[61] Pieper, M. L., Manolakis, D., Lockwood, R., Cooley, T., Armstrong, P., & Jacobson, J. (2011, September). Hyperspectral detection and discrimination using the ACE algorithm. In Proc. SPIE (Vol. 8158, pp. 815807-815807).
[62]Manolakis, D. G., Siracusa, C., Marden, D., & Shaw, G. A. (2001, August). Hyperspectral adaptive matched-filter detectors: Practical performance comparison. In Aerospace/Defense Sensing, Simulation, and Controls (pp. 18-33). International Society for Optics and Photonics.
[63] Geng, X., Ji, L., Sun, K., & Zhao, Y. (2014). CEM: More bands, better performance. IEEE Geoscience and Remote Sensing Letters, 11(11), 1876-1880.
[64] West, J. E., Messinger, D. W., Ientilucci, E. J., Kerekes, J. P., & Schott, J. R. (2005, June). Matched filter stochastic background characterization for hyperspectral target detection. In Defense and Security (pp. 1-12). International Society for Optics and Photonics.
[65] AVIRIS-Airborne Visible/Infrared Imaging Spectrometer. Retrieved April 24, 2017, from https://aviris.jpl.nasa.gov/
[66] Roger, R. E., & Arnold, J. F. (1996). Reliably estimating the noise in AVIRIS hyperspectral images. *International Journal of Remote Sensing*, *17*(10), 1951-1962.
[67] Hyperspectral Remote Sensing Scenes. Retrieved April 24, 2017, from http://www.ehu.eus/ccwintco/index.php?title=Hyperspectral_Remote_Sensing_Scenes

[68] Veganzones, M. A., Tochon, G., Dalla-Mura, M., Plaza, A. J., & Chanussot, J. (2014). Hyperspectral image segmentation using a new spectral unmixing-based binary partition tree representation. *IEEE Transactions on Image Processing*, *23*(8), 3574-3589.

CURRICULUM VITAE

Graduate College
University of Nevada, Las Vegas

Ruixing Li

E-mail Address:
lir1@unlv.nevada.edu

Degrees:
Bachelor of Engineering, Information Engineering, 2007
South China Normal University, China

Master of Science, Electrical Engineering, 2017
University of Nevada, Las Vegas

Thesis Title: Improving Hyperspectral Subpixel Target Detection Using Hybrid Detection Space

Thesis Examination Committee:

Chair, Dr. Shahram Latifi
Committee Member, Dr. Sahjendra Singh
Committee Member, Dr. Pushkin Kachroo
Graduate College Representative, Dr. Laxmi Gewali